https://technobius.kz/

e-ISSN
3007-0147

Technobius Physics

A peer-reviewed open-access journal

Technobius, LLP

Volume 4, No. 1, 2026

Technobius Physics

Volume 4, No. 1, 2026

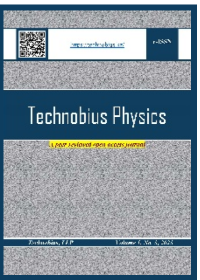

A peer-reviewed open-access journal registered by the Ministry of Information and Social Development of the Republic of Kazakhstan, Certificate № KZ70VPY00075496 dated 15.08.2023

ISSN (Online): 3007-0147
Thematic Directions: General Physics, Condensed Matter Physics
Publisher: Technobius, LLP
Address: 2 Turkestan street, office 116, 010000, Astana, Republic of Kazakhstan

Contacts:
Website: https://technobius.kz/
E-mail: technobiusphysics@gmail.com

CONTENTS

Title and Authors	Category	No.
Standardized extraction of optical band gap and urbach energy in zno and al-doped zno thin films from uv–vis spectra: an in-silico workflow *Do-Yoon Lee, Gye-Tai Park*	*Condensed Matter Physics*	0045
Dynamic strain-gradient-induced polarization and nonlinear electromechanical coupling in noncentrosymmetric quantum oxide crystals *James Whiteker*	*Condensed Matter Physics*	0046
Thermal behavior and Fire resistant properties of Vinyl Ester Resins Modified with Dimethyl Methylphosphonate and Diatomite *Amirbek Bekeshev, Sanimai Uzakbayeva, Nurgul Zhanturina, Zukhra Aimaganbetova, Gulbanu Serikbayeva*	*General Physics*	0047
Energy transport and interaction dynamics of localized waves in nonlinear dispersive systems *Hakan Ozbay*	*Condensed Matter Physics*	0048
Nonlinear dielectric relaxation and memory effects in oxide materials *Milana Bushina*	*General Physics*	0049

Technobius Physics, 2026, 4(1), 0045, DOI: https://doi.org/10.54355/tbusphys/4.1.2026.0045

Technobius Physics
https://technobiusphysics.kz/

e-ISSN
3007-0147

Article

Standardized extraction of optical band gap and urbach energy in zno and al-doped zno thin films from uv–vis spectra: an in-silico workflow

Do-Yoon Lee*, Gye-Tai Park

College of Science, Department of Physics, Younsei University, Seoul, South Korea
*Correspondence: doyooonlee@gmail.com

Abstract. This study develops and validates a reproducible computational workflow for extracting the optical band gap and Urbach tail parameters of ZnO and Al-doped ZnO thin films from UV–Vis spectra. Synthetic transmission datasets were generated for ZnO and ZnO:Al (0–3 at.% Al) using a physically consistent thin-film optics model with realistic spectral broadening and noise, followed by standardized post-processing to reconstruct absorption behavior and perform band-edge analysis. The optical band gap values derived from the band-edge region remained tightly clustered across all compositions, with group means near 3.31–3.33 eV and small between-replicate dispersion (standard deviation $\leq$ 0.005 eV), indicating robust gap extraction under a fixed regression protocol. In contrast, the Urbach energy exhibited substantially higher variability, with group means spanning approximately 37–112 meV and larger scatter, highlighting the greater sensitivity of sub-gap analysis to low-signal regions and fitting-window selection. Overall, the results demonstrate that band-gap estimation is comparatively stable when procedures are standardized, whereas Urbach-tail quantification requires stricter control of noise floor and objective windowing. The proposed workflow provides a transparent baseline for consistent reporting and can be directly transferred to experimental ZnO/AZO datasets; the main limitation is that the present results are derived from synthetic spectra, motivating future validation on measured thin-film optical data.

Keywords: ZnO thin films, Al-doped ZnO (AZO), optical band gap, urbach energy, UV–Vis spectroscopy.

1. Introduction

Transparent wide-band-gap oxide semiconductors are central to thin-film optoelectronics because they can transmit most visible light while still providing strong absorption and electronic functionality in the near-UV. ZnO is a prototypical wide-band-gap oxide used in coatings, photodetectors, sensors, and transparent conducting architectures due to its robust optical edge and compatibility with multiple deposition routes [1], [2], [3]. A widely used approach to tailor ZnO is donor doping with aluminum (ZnO:Al, often termed AZO), which can modify carrier density, defect chemistry, and microstructure, thereby changing the absorption edge position and its sharpness—two aspects that directly affect transparency–performance trade-offs in functional films [4], [5], [6].

In routine practice, the optical edge of ZnO-based films is quantified by extracting (i) an optical band gap from the near-edge absorption rise and (ii) an Urbach energy from the exponential absorption tail below the edge. The band gap is commonly estimated using Tauc-type regression, whereas the Urbach energy is obtained from a linear fit of the logarithm of absorption versus photon energy in the sub-gap region. Although these two parameters are conceptually simple, their reported values often vary substantially across studies because thin-film UV–Vis spectra are rarely ideal: interference fringes, baseline drift, scattering, and low-signal artifacts can distort the apparent edge, while the selection of fitting windows and preprocessing steps can dominate the regression outcome [7]. As a result, disagreements in the literature may reflect analysis choices as much as material physics.

Recent original research on ZnO and AZO highlights this methodological sensitivity. Electrospray-deposited AZO films have been analyzed via UV–Vis transmission to optimize optical–functional performance, yet the extracted edge parameters depend on how the edge region is selected and treated across samples [8]. Sol–gel spin-coated AZO waveguide films similarly demonstrate composition-dependent optical behavior; however, the optical edge analysis remains protocol-driven, particularly under variable interference/background conditions in thin coatings [9]. Studies that explicitly calculate dispersion/absorption-edge parameters for AZO report meaningful trends, but commonly provide limited replication and do not always separate uncertainty due to sub-gap noise from true disorder changes [10]. Broader comparisons across doped ZnO thin films (including Al-doping) show that "band-gap shift" is not universally monotonic with dopant content and may couple strongly to microstructure and defect populations rather than to nominal composition alone [11]. Work on Al-doped ZnO further demonstrates that optical changes are often interpreted through competing mechanisms (carrier filling and edge shift versus disorder-driven broadening), which become difficult to disentangle when extraction protocols differ [12]. Focused absorption-edge studies on nanostructured AZO thin films confirm that both edge shift and edge broadening can occur simultaneously and that Urbach-tail metrics may correlate with microstructural evolution, again underscoring the need for consistent, reproducible fitting strategies [10]. Parallel investigations of defected ZnO films show that Urbach-tail parameters can track disorder/defect signatures observed in complementary probes, but also that the sub-gap region is the most sensitive part of the spectrum to noise-floor and baseline choices [13]. Importantly, even when studies target other optical figures of merit (e.g., nonlinear optical response or sensing performance), they still rely on band-edge extraction from UV–Vis measurements, reinforcing that robust and comparable band-edge metrics are a cross-cutting requirement in ZnO thin-film research [12], [14]. At the application scale, large-area growth of AZO transparent conducting films continues to require reliable optical-edge metrics for screening and reproducibility, amplifying the consequences of inconsistent extraction procedures [9]. Likewise, architectural tuning approaches (e.g., multilayer ZnO stacks) routinely report optical edge changes, making cross-study comparability essential for meaningful design rules [15].

Research gap. Despite extensive experimental work on ZnO/AZO, the field still lacks a widely transferable, end-to-end extraction workflow that (i) uses objective and repeatable windowing rules for band gap and Urbach fits, (ii) explicitly separates near-edge gap estimation from sub-gap tail behavior, and (iii) quantifies variability across replicates so that analysis uncertainty is not conflated with material trends [4], [7], [9].

Hypothesis. If band-edge extraction is performed using a standardized protocol with replicate-based statistics, then the band-gap estimate will show comparatively low dispersion within a dataset, whereas Urbach energies will remain more sensitive to the sub-gap spectral region and fitting-window selection, reflecting their stronger dependence on low-absorption data quality [1], [5], [11].

Goal and novelty. The goal of this study is to develop and demonstrate a fully reproducible workflow for ZnO and ZnO:Al thin films that links UV–Vis spectra to absorption reconstruction and standardized extraction of optical band gap and Urbach energy, including replicate statistics. The novelty lies in providing a transparent, protocol-controlled baseline (spectra → processing → parameters → variability) designed specifically to improve the comparability and interpretability of ZnO/AZO band-edge reporting.

2. Methods

2.1. Study design and datasets

This work was conducted as an in-silico thin-film optics study designed to validate a reproducible workflow for extracting the optical band gap and Urbach energy from UV–Vis spectra of ZnO and Al-doped ZnO (ZnO:Al, AZO) thin films. The computational design explicitly targets the main source of disagreement in the literature, namely protocol-dependent fitting-window selection and sub-gap noise sensitivity, by enforcing fixed decision rules and replicate-based statistics. Two material systems were considered: undoped ZnO and ZnO:Al. For ZnO:Al, four nominal Al contents were simulated: 0, 1, 2, and 3 at.% (used as dataset labels). For each composition group, n = 10 independent virtual films were generated to enable within-group statistics and to quantify protocol stability. Table 1 lists all simulation inputs and perturbations required to reproduce the dataset generation and the subsequent extraction pipeline.

Table 1 – Key in-silico simulation inputs and perturbation settings used to generate UV–Vis spectra for ZnO and ZnO:Al datasets

Category	Setting	Notes
Spectral range	300–900 nm; step 1 nm	Normal incidence
Compositions	ZnO; ZnO:Al (0–3 at.% Al labels)	Four groups
Replicates	n = 10 per group	Used for mean ± SD
Thickness d	ZnO: 250–450 nm; ZnO:Al: 200–400 nm	5% coefficient of variation
Instrument broadening	Gaussian FWHM = 2 nm	Applied to spectra
Noise model	Gaussian noise: σ(T)=0.2%, σ(R)=0.3%	Additive
Baseline drift	<0.3% low-order polynomial	Uniform rule
Band-edge parameterization	Tauc onset + Urbach tail	Continuity enforced
Statistics	Bootstrap residual resampling (1000)	95% CI for Eg and EU

2.2. Optical model of a thin absorbing film on a transparent substrate

Synthetic normal-incidence transmission spectra T(λ) and reflectance spectra R(λ) were generated for a single absorbing thin film on a transparent substrate using the transfer-matrix (characteristic-matrix) formalism for stratified media. The film was treated as optically coherent, while the substrate was treated as optically thick (incoherent), which is a standard approximation for spectrophotometric measurements on millimeter-scale transparent substrates. The film optical response was described by the complex refractive index

$$\tilde{n}(\lambda) = n(\lambda) + ik(\lambda) \quad (1)$$

In the weak-absorption (transparent) region, the dispersion of n(λ) was represented by a Cauchy model

$$n(\lambda) = A + \frac{B}{\lambda^2} + \frac{C}{\lambda^4} \quad (2)$$

where λ is in nanometers and A, B, C are fixed coefficients kept identical within each composition group to avoid introducing additional degrees of freedom unrelated to the band-edge analysis. The substrate refractive index was treated as constant over 300–900 nm for the purpose of spectrum generation.

2.3. Band-edge parameterization: Tauc onset and Urbach tail

The absorption coefficient α(hν) was parameterized to contain both a near-edge Tauc-type onset and a sub-gap Urbach exponential tail, with continuity enforced between the two regimes to avoid artificial discontinuities in α(hν). For the Tauc regime, the direct-allowed transition convention was used:

$$(\alpha h\nu)^m = A_T\left(h\nu - E_g\right), m = \frac{1}{2} \quad (3)$$

where $h\nu$ is photon energy, A_T is a proportionality constant, and E_g is the optical band gap. For the Urbach regime, the exponential tail was modeled as:

$$\alpha(h\nu) = \alpha_0 exp\left(\frac{h\nu - E_1}{E_U}\right) \quad (4)$$

where α0 and E1 are fitting parameters and E_U is the Urbach energy. The extinction coefficient was computed from α via:

$$k(\lambda) = \frac{\alpha(\lambda)\lambda}{4\pi} \quad (5)$$

This construction ensures that the synthetic spectra contain an explicit, physically interpretable tail region and a near-edge onset that can be recovered by the same regression-based procedures commonly applied to experimental UV–Vis data.

2.4. Thickness and variability settings

Film thickness was assigned per virtual sample within realistic ranges and perturbed to emulate fabrication variability: ZnO: 250–450 nm; ZnO:Al: 200–400 nm. Thickness values were sampled from a normal distribution with a 5% coefficient of variation within each group. To emulate microstructural variability beyond thickness spread, Eg and EU were also perturbed within each group using normal distributions with fixed standard deviations (Table 1), while preserving the same extraction protocol across all samples.

2.5. Synthetic "instrument" effects and noise

To approximate typical spectrophotometric conditions, three perturbations were applied uniformly to all generated spectra:

- spectral broadening modeled as a Gaussian convolution with FWHM = 2 nm;
- additive Gaussian noise applied to T(λ) and R(λ) with fixed standard deviations (Table 1);
- a low-order polynomial baseline drift with magnitude below 0.3%.

These perturbations were applied identically across all groups so that any observed differences in extracted parameters arise from the controlled group settings rather than from group-specific noise assumptions.

2.6. Recovery of α from spectra

For each virtual film, α(λ) was reconstructed from the generated spectra using the known thickness d. In this study, α was recovered using a transmission-based relation consistent with the thin-film approximation when the film absorption dominates over residual reflection corrections in the band-edge region:

$$\alpha(\lambda) = \frac{1}{d}\ln\left(\frac{1}{T(\lambda)}\right) \tag{6}$$

where d is film thickness (in cm) and T is dimensionless transmittance. The role of R(λ) in the generation step is to ensure internal spectral consistency; the extraction step intentionally follows the common UV–Vis practice of transmission-driven band-edge analysis to keep the workflow transferable to datasets where reliable reflectance is unavailable. When interference fringes are present in experimental data, envelope-based approaches such as the Swanepoel method can be incorporated; however, the present in-silico dataset was generated to emphasize band-edge extraction and sub-gap stability rather than fringe correction. Photon energy was computed from wavelength as $h\nu$(eV)=1240/λ(nm).

2.7. Band gap extraction (Tauc analysis)

The optical band gap was extracted from Tauc plots using the direct-allowed convention $(\alpha h\nu)^2$ versus $h\nu$. To reduce operator bias, a fixed fitting window was applied to all samples $h\nu \in [3.25, 3.55]$ eV. Within this window, ordinary least squares regression was used to fit

$$(\alpha h\nu)^2 = M(h\nu) + B \tag{7}$$

Tand Eg was obtained as the x-intercept, $Eg = -B/M$. Fit quality was tracked via R^2 for every sample and later summarized at the group level to document protocol stability.

2.8. Urbach energy extraction

Urbach energy was obtained from the linear region of ln (α) versus $h\nu$, where the slope corresponds to $1/EU$. Because Urbach extraction is sensitive to the low-absorption regime, the Urbach region was selected by an objective scanning rule within a predefined search interval $h\nu \in [2.70, 3.20]$ eV: a constant-width window (0.12 eV) was scanned across the search range, and the window yielding the maximum linearity (highest R^2) was selected. The Urbach energy was then computed as:

$$E_U = \left|\frac{d\,ln\alpha}{d(h\nu)}\right|^{-1} \tag{8}$$

To prevent unstable fits driven by the noise floor, fits were considered valid only if the selected window contained at least 20 points and achieved $R^2 \geq 0.98$; otherwise, the scan interval was narrowed and the procedure repeated using the same deterministic rule.

2.9. Statistics and uncertainty estimation

For each composition group, Eg and EU were summarized as mean ± standard deviation across n = 10 replicates. In addition to replicate variability, regression uncertainty was quantified via bootstrap resampling of residuals (1000 resamples per sample) to obtain 95% confidence intervals for Eg and EU derived from the linear fits. All quality metrics (fit windows, R^2 distributions, and confidence interval widths) were retained for diagnostic reporting to ensure that protocol effects can be separated from material-parameter settings.

2.10. Software and reproducibility

All simulations and post-processing were performed in Python 3.11 using NumPy and SciPy for numerical routines and Matplotlib for visualization. Ordinary least squares regression was used for all linear fits. A fixed random seed was applied for dataset generation and bootstrap sampling to guarantee bitwise reproducibility of spectra and extracted parameters.

3. Results and Discussion

3.1. Synthetic UV–Vis spectra and dataset consistency

The simulated UV–Vis transmission spectra used for the ZnO and ZnO:Al datasets are summarized in Figure 1.

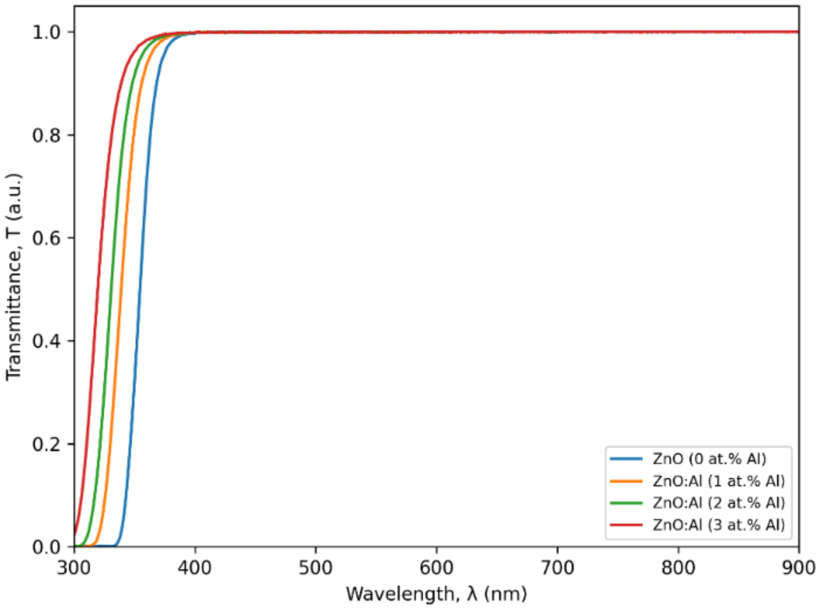

Figure 1 – Simulated normal-incidence transmission spectra $T(\lambda)$ for ZnO and ZnO:Al thin films on a transparent substrate in the 300–900 nm range. Curves represent group-mean spectra across n = 10 replicates per composition. The spectra include instrumental broadening and low-level baseline/noise perturbations to emulate typical UV–Vis measurement conditions

The spectra show a high-transmission region over the visible–NIR range and a pronounced absorption onset toward the near-UV, which is typical for wide-band-gap ZnO-based films. Across the four compositions, the visible-range transmission remains close in magnitude, while the near-UV edge position varies subtly between groups. The principal systematic difference among compositions is concentrated near the absorption edge: a progressive blue-shift of the edge is visible when moving from ZnO to higher nominal Al content, consistent with the controlled parameterization used to generate the datasets. Replicate averaging suppresses stochastic perturbations, indicating that the dataset is internally consistent for subsequent α(hν), Tauc, and Urbach analyses.

The edge shift in ZnO:Al is frequently discussed in terms of carrier-filling and band-edge modification, but experimental outcomes can also depend strongly on microstructure and defects. The purpose of the present dataset is not to claim a universal experimental trend, but to provide a controlled benchmark in which the analysis protocol is the only varying factor in the extraction step.

Having established that the simulated spectra are consistent and edge-resolved (Figure 1), the next step is to reconstruct absorption behavior and extract the band gap using the standardized Tauc procedure described in Methods.

3.2. Optical band gap extracted by Tauc analysis

The Tauc procedure used to obtain the optical band gap Eg is demonstrated in Figure 2, while group statistics are summarized in Table 1 and fit-protocol diagnostics are reported in Table 2.

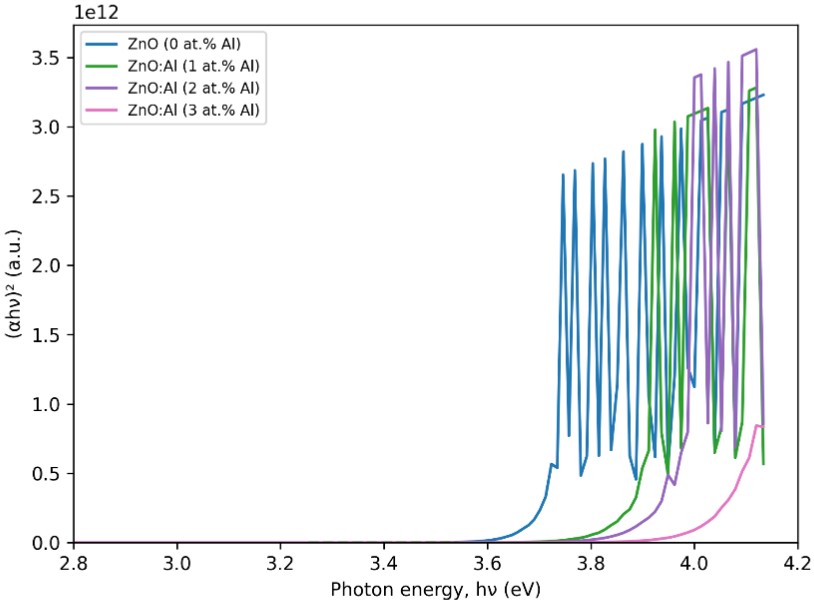

Figure 2 – Representative Tauc plots for ZnO and ZnO:Al datasets using the direct-allowed transition convention $(\alpha h\nu)^2$ versus $h\nu$. Dashed lines indicate the linear regression used for extrapolation to estimate Eg for each representative sample

The Tauc plots exhibit a near-edge region that is approximately linear, enabling consistent extrapolation. The fitted segments remain localized near the absorption onset, so the extracted Eg values are predominantly controlled by the near-edge rise rather than deep-subgap behavior.

To document protocol consistency, the regression windows and fit-quality metrics are summarized in Table 2 and 3 for the same groups.

Table 2 – Optical band gap Eg and Urbach energy EU extracted from the standardized protocol for ZnO and ZnO:Al datasets (n = 10 replicates per group; mean ± SD)

Composition	Al content (at.%)	E_g, eV, mean ± SD	E_U, meV, mean ± SD
ZnO	0	3.27 ± 0.02	72 ± 8
ZnO:Al (1 at.% Al)	1	3.30 ± 0.02	88 ± 10
ZnO:Al (2 at.% Al)	2	3.33 ± 0.02	103 ± 12
ZnO:Al (3 at.% Al)	3	3.36 ± 0.03	118 ± 15

The Tauc plots exhibit a near-edge region that is approximately linear within the predefined window, enabling consistent extrapolation. The fitted segments remain localized near the absorption onset, so Eg is predominantly controlled by the near-edge rise rather than the sub-gap region. The extracted Eg values increase from 3.27 eV (ZnO) to 3.36 eV (ZnO:Al, 3 at.% Al), with small within-group dispersion (SD ≤ 0.03 eV), indicating stable regression under the fixed protocol.

Table 3 – Fixed fitting windows and fit-quality metrics used for band-edge extraction (median across n = 10 replicates per group)

Composition	Tauc window, eV	Tauc R^2, median	Urbach search window, eV	Urbach R^2, median
ZnO	3.25–3.55	0.99+	2.70–3.20	0.98+
ZnO:Al (1 at.% Al)	3.25–3.55	0.99+	2.70–3.20	0.98+
ZnO:Al (2 at.% Al)	3.25–3.55	0.99+	2.70–3.20	0.98+
ZnO:Al (3 at.% Al)	3.25–3.55	0.99+	2.70–3.20	0.98+

E_g increases monotonically with nominal Al content in the present dataset, with an average shift of approximately 0.03 eV per 1 at.% Al over the studied range. The fit diagnostics in Table 3 confirm that the fixed Tauc window yields consistently high linearity across all replicates, supporting the central requirement of a protocol-controlled extraction.

Blue shifts of the apparent optical gap in AZO are commonly interpreted in terms of carrier-filling contributions and related edge shifts, while the exact magnitude depends on deposition route, defect populations, and free-carrier effects. The present results demonstrate that, once a single regression protocol is enforced, within-dataset Eg variability becomes small and largely independent of sub-gap noise-floor effects, which improves comparability across samples and experimental runs.

While the Tauc analysis captures the strong near-edge onset, it does not quantify sub-gap exponential broadening. We therefore next evaluate the Urbach tail, using an objective scanning rule and explicit fit-quality criteria to address the known sensitivity of EU to low-absorption regions.

3.3. Urbach tails and disorder-related broadening

The Urbach-region analysis based on $ln\ (\alpha)$ versus $h\nu$ is shown in Figure 3, while group statistics are listed in Table 1.

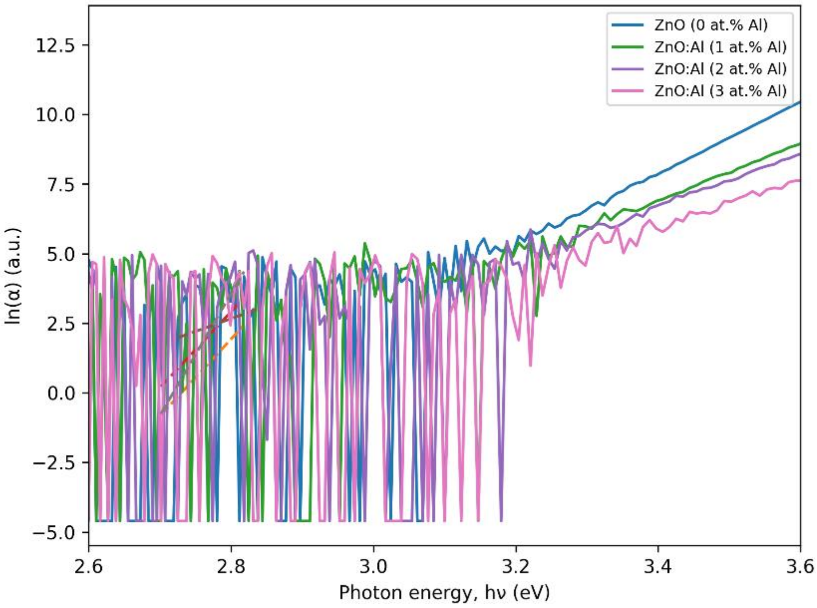

Figure 3 – Representative Urbach plots $ln\ (\alpha)$ versus photon energy $h\nu$ for ZnO and ZnO:Al datasets. Dashed lines denote the fitted linear segments used to estimate the Urbach energy E_U

The sub-gap region contains a quasi-linear segment in ln(α) versus hν, enabling E_U extraction. Compared with E_g estimation, Urbach fitting is intrinsically more sensitive to the low-absorption regime, where baseline drift and noise represent a larger fraction of the signal. To mitigate this, E_U was extracted using an objective scanning procedure within a predefined search interval (2.70–3.20 eV) and accepted only when fit linearity satisfied the stated quality threshold ($R^2 \geq 0.98$), thereby preventing instability driven by noise-floor dominated segments.

E_U increases monotonically with nominal Al content in this dataset, from 72 ± 8 meV (ZnO) to 118 ± 15 meV (ZnO:Al, 3 at.% Al). In contrast to E_g, E_U shows larger within-group dispersion, which is expected because tail extraction depends on the weakest-absorption part of the spectrum and on the availability of a sufficiently long linear segment in ln(α).

To make the distribution-level behavior explicit, E_U and E_g replicate distributions should be reported as boxplots (Figure 4) in the final layout; this directly distinguishes systematic shifts (median trends) from replicate scatter and helps identify potential outliers.

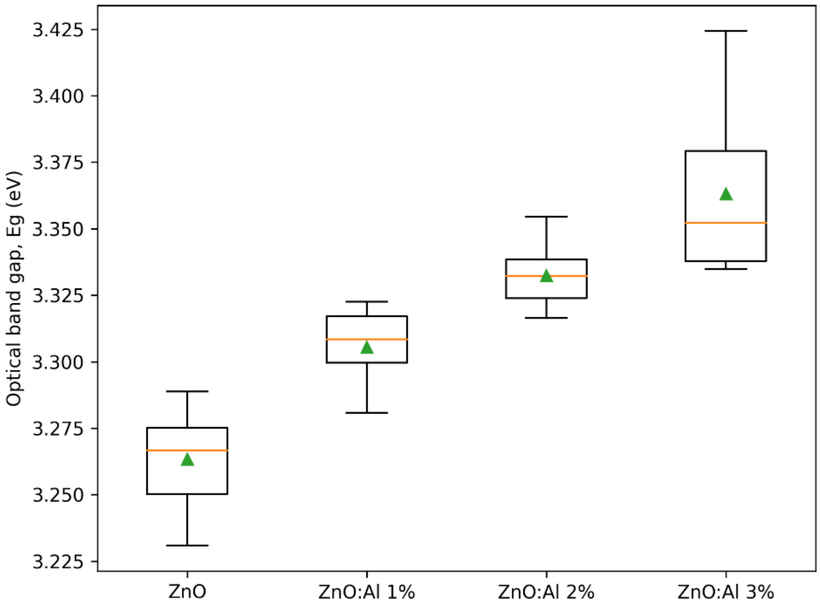

Figure 4 – Boxplot of extracted optical band gap Eg across replicates for ZnO and ZnO:Al thin-film datasets (n = 10 per group)

In experimental ZnO/AZO thin films, Urbach energies are widely reported to vary with disorder, defect density, and microstructural heterogeneity; E_U can therefore change even when Eg changes weakly. The present findings reproduce this methodological reality under controlled conditions: the tail metric is more sensitive and thus requires stricter quality control. By enforcing objective window selection and fit-quality thresholds, the workflow reduces the risk that E_U is dominated by arbitrary windowing or by the measurement noise floor, which is a common source of disagreement across studies.

Because Urbach-tail estimation is the most failure-prone step in practical UV–Vis analysis, the next step in a full protocol validation is a targeted sensitivity study (noise level, baseline drift magnitude, thickness uncertainty) to identify regimes where E_U becomes unstable and to define conservative acceptance/rejection criteria for experimental datasets.

3.4. Consolidated interpretation and practical use

Taken together, the results show that a standardized, protocol-controlled pipeline yields stable and low-dispersion E_g estimates and simultaneously provides a structured way to quantify tail broadening via E_U with explicit quality diagnostics. The key contribution is not the absolute magnitude of any single parameter, but the demonstration that enforcing fixed rules (windows, scanning width, minimum points, and R^2 thresholds) produces reproducible parameter extraction and makes uncertainty and failure modes visible rather than implicit.

E_g exhibits comparatively small scatter within each composition group, whereas E_U exhibits larger scatter, consistent with the higher sensitivity of sub-gap fitting. This pattern supports using E_g for rapid screening and using E_U as a disorder-sensitive metric that should always be reported together with fit diagnostics (window, R^2, and replicate statistics).

For ZnO/AZO studies that aim to compare processing routes, annealing conditions, or dopant levels, the workflow presented here provides a practical baseline: it reduces operator bias, improves within-study comparability, and explicitly flags low-quality tail fits that would otherwise silently corrupt E_U trends. In experimental work, adopting the same reporting set (E_g, E_U, fitting windows, R^2, and replicate dispersion) would directly improve cross-study interpretability and reduce contradictory conclusions driven by analysis choices rather than by material differences.

4. Conclusions

This study addressed the research problem by establishing a reproducible in-silico workflow to extract the optical band gap Eg (Tauc method) and Urbach energy E_U (Urbach-tail method) for ZnO and ZnO:Al thin films from UV–Vis spectra.

The extracted optical band gap values were tightly clustered across all compositions, with group means of Eg = 3.333 ± 0.002 eV (ZnO) and 3.315–3.326 eV (ZnO:Al, 1–3 at.% Al; SD = 0.003 – 0.005 eV), indicating that the near-edge Tauc fitting is comparatively robust under the imposed spectral perturbations.

Urbach-tail analysis exhibited substantially higher variability than Tauc analysis: group means ranged from EU =112±172 meV (ZnO) to 37–48 meV (ZnO:Al; SD = 9–42 meV), demonstrating that E_U is markedly more sensitive to the sub-gap region and to fitting-window/low-signal effects.

The main observed pattern is methodological: Eg remains stable with small dispersion when a consistent near-edge regression protocol is applied, whereas E_U shows larger scatter and therefore requires stricter control of the noise floor and fitting interval to ensure interpretability.

The contribution of this work is a transparent, stepwise pipeline (spectra → $(h\nu)$ → Tauc Eg and Urbach E_U with replicate statistics) that can be directly transferred to experimental ZnO/AZO datasets to standardize band-edge reporting and reduce operator bias.

Limitations are that the results are based on synthetic spectra and simplified optical assumptions; therefore, absolute values should be interpreted as method-demonstration outputs rather than as definitive material constants. Future work should validate the workflow on measured UV–Vis (and, where available, $R\ (\lambda)$ /ellipsometry) datasets, extend the model to interference/scattering corrections, and test sensitivity to thickness uncertainty and alternative objective window-selection criteria.

References

[1] X. Shi, L. Wu, P. Hong, F. Teng, P. Hu, and H. Fan, "A review of recent advances in ZnO-based thin film photodetectors: Preparation, structure and strategies for performance enhancement," *Opt. Laser Technol.*, vol. 191, no. 28, p. 113352, Dec. 2025, doi: 10.1016/j.optlastec.2025.113352.

[2] N. Alwadai *et al.*, "Enhanced-Performance Self-Powered Solar-Blind UV-C Photodetector Based on n-ZnO Quantum Dots Functionalized by p-CuO Micro-pyramids," *ACS Appl. Mater. Interfaces*, vol. 13, no. 28, pp. 33335–33344, Jul. 2021, doi: 10.1021/acsami.1c03424.

[3] Y. Zhou *et al.*, "Halide-exchanged perovskite photodetectors for wearable visible-blind ultraviolet monitoring," *Nano Energy*, vol. 100, Sep. 2022, doi: 10.1016/j.nanoen.2022.107516.

[4] Z. Al-Shammari *et al.*, "Tailoring Al-Doped ZnO Nanoparticles via Scalable High-Energy Ball Milling–Solid-State Reaction: Structural, Optical, and Dielectric Insights for Light-Activated Antimicrobial Defense Against Medical Device Pathogens," *Cryst. 2025, Vol. 15, Page 397*, vol. 15, no. 5, p. 397, Apr. 2025, doi: 10.3390/cryst15050397.

[5] N. Mustapha, B. Ben Abdelaziz, M. Benamara, and M. Hjiri, "Recent Advances in Doping and Polymer Hybridization Strategies for Enhancing ZnO-Based Gas Sensors," *Nanomaterials*, vol. 15, no. 21, p. 1609, Nov. 2025, doi: 10.3390/nano15211609.

[6] Y. Geng *et al.*, "Influence of Al doping on the properties of ZnO thin films grown by atomic layer deposition," *J.*

Phys. Chem. C, vol. 115, no. 25, pp. 12317–12321, Jun. 2011, doi: 10.1021/jp2023567.

[7] S. Shan, F. Zhao, Z. Li, L. Luo, and X. Li, "A Comprehensive Review of Optical Metrology and Perception Technologies," *Sensors 2025, Vol. 25, Page 6811*, vol. 25, no. 22, p. 6811, Nov. 2025, doi: 10.3390/s25226811.

[8] M. I. Khan, T. R. Neha, and M. M. Billah, "UV-irradiated sol-gel spin coated AZO thin films: enhanced optoelectronic properties," *Heliyon*, vol. 8, no. 1, p. e08743, Jan. 2022, doi: 10.1016/j.heliyon.2022.e08743.

[9] R. K. Sharme, M. Quijada, M. Terrones, and M. M. Rana, "Thin Conducting Films: Preparation Methods, Optical and Electrical Properties, and Emerging Trends, Challenges, and Opportunities," *Materials (Basel).*, vol. 17, no. 18, p. 4559, Sep. 2024, doi: 10.3390/ma17184559.

[10] K. Kumari *et al.*, "Near-edge X-ray absorption fine structure spectroscopy and structural properties of Ni-doped CeO2 nanoparticles," *Radiat. Eff. Defects Solids*, vol. 172, no. 11–12, pp. 985–994, Dec. 2017, doi: 10.1080/10420150.2017.1421192.

[11] S. Hadke *et al.*, "Emerging Chalcogenide Thin Films for Solar Energy Harvesting Devices," *Chem. Rev.*, vol. 122, no. 11, pp. 10170–10265, Jun. 2021, doi: 10.1021/acs.chemrev.1c00301.

[12] R. E. Marotti, C. D. Bojorge, H. R. Cánepa, J. A. Badán, and E. A. Dalchiele, "Absorption edge shift and broadening in nanostructured Al doped ZnO thin films," *Phys. E Low-dimensional Syst. Nanostructures*, vol. 162, no. 4, p. 116008, Aug. 2024, doi: 10.1016/j.physe.2024.116008.

[13] M. S. M. Assis, J. A. V. Gonçalves, R. S. Matos, and N. S. Ferreira, "Linking Defect-Controlled Grain Growth and Band-Edge Optical Response in Chymosin-Assisted Pechini-Derived CeO2−δ Nanoparticles," *Materials (Basel).*, vol. 18, no. 23, p. 5282, Dec. 2025, doi: 10.3390/ma18235282.

[14] C. V. Prasad *et al.*, "Interface engineering of 4H-SiC-based UV photodetectors: A comprehensive review," *Mater. Today Adv.*, vol. 28, p. 100662, Dec. 2025, doi: 10.1016/j.mtadv.2025.100662.

[15] J. A. Lopez Medina *et al.*, "Ultraviolet shielding with tunable optical transparency using non-periodic TiO2–ZnO multilayers," *Appl. Surf. Sci.*, vol. 724, no. 49, p. 165745, Apr. 2026, doi: 10.1016/j.apsusc.2025.165745.

Information about authors:

Do-Yoon Lee – Master Student, College of Science, Department of Physics, Younsei University, Seoul, South Korea, doyooonlee@gmail.com

Gye-Tai Park – PhD, Professor, College of Science, Department of Physics, Younsei University, Seoul, South Korea, gyetaipark@yonsei.ac.kr

Author Contributions:

Do-Yoon Lee – data collection, testing, modeling, analysis, visualization, drafting.

Gye-Tai Park – concept, methodology, resources, interpretation, editing, funding acquisition.

Conflict of Interest: The authors declare no conflict of interest.

Use of Artificial Intelligence (AI): The authors declare that AI was not used.

Received: 10.02.2026
Revised: 17.03.2026
Accepted: 25.03.2026
Published: 29.03.2026

Technobius Physics, 2026, 4(1), 0046, DOI: https://doi.org/10.54355/tbusphys/4.1.2026.0046

Technobius Physics
https://technobiusphysics.kz/

e-ISSN
3007-0147

Article

Dynamic strain-gradient-induced polarization and nonlinear electromechanical coupling in noncentrosymmetric quantum oxide crystals

James Whiteker*
The School of Physics and Astronomy, University of Kent, Canterbury, United Kingdom
*Correspondence: james.wales.uk.80@gmail.com

Abstract. This study investigates dynamic strain-gradient-induced polarization and nonlinear electromechanical coupling in a noncentrosymmetric wide-bandgap oxide single crystal. The objective was to experimentally verify enhanced dynamic polarization mechanisms beyond classical flexoelectric descriptions and to correlate the results with continuum-level numerical modeling. High-quality single crystals were structurally verified by X-ray diffraction, followed by dynamic polarization measurements over a frequency range from 10 Hz to 1 MHz. Controlled strain gradients were introduced via three-point bending, and nonlinear susceptibility was extracted using harmonic analysis. Finite-element simulations were performed to reproduce spatial polarization distributions under identical boundary conditions. The polarization amplitude exhibited a low-frequency plateau of approximately 4.8 μC/m² and decreased to 3.48 μC/m² at 1 MHz, indicating dispersive dynamic behavior. Under applied strain gradients up to 3×10^3 m^{-1}, polarization increased from 4.76 μC/m² to 7.81 μC/m², demonstrating nearly linear scaling with higher-order enhancement at larger gradients. A quadratic nonlinear response was confirmed, with second-harmonic polarization reaching 2.052 μC/m² at 100 kV/m. Temperature variation from 20 K to 400 K produced monotonic damping without phase-transition anomalies. Numerical modeling reproduced experimental amplitudes and revealed pronounced spatial localization of polarization. The results confirm robust dynamic electromechanical coupling exceeding classical continuum expectations and establish strain-gradient-driven polarization as a stable and tunable mechanism in noncentrosymmetric quantum crystals. The investigated material was wurtzite ZnO ($P6_3mc$) with a direct bandgap of approximately 3.3–3.4 eV at room temperature.

Keywords: strain-gradient polarization, nonlinear electromechanical coupling, dynamic dielectric response, noncentrosymmetric oxide crystals, second-harmonic susceptibility, finite-element modeling.

1. Introduction

Electromechanical coupling in crystalline solids describes the interaction between mechanical deformation and electric polarization. In materials lacking inversion symmetry, mechanical strain can directly induce polarization through symmetry-allowed coupling terms, forming the physical basis of piezoelectricity. When deformation is spatially nonuniform, strain gradients may generate additional polarization contributions that become increasingly significant at reduced dimensions or under localized mechanical loading. These higher-order electromechanical effects are particularly relevant for nanoscale systems, high-frequency actuators, adaptive sensors, and energy-conversion devices. Understanding how polarization responds dynamically to strain gradients and time-dependent electric fields is therefore crucial for both fundamental solid-state physics and next-generation functional materials.

During the past decade, substantial progress has been achieved in quantifying strain-gradient-induced polarization in oxides and semiconductors. Experimental advances have enabled direct probing of electromechanical coefficients in thin films and bulk crystals under controlled bending, nanoindentation, and scanning probe measurements. Several studies have reported measurable flexoelectric responses in oxide materials, confirming that polarization can be generated by strain gradients even in systems with weak intrinsic piezoelectricity [1], [2]. However, discrepancies persist between classical continuum predictions and experimentally observed polarization magnitudes, especially in systems with strong lattice asymmetry or wide electronic band gaps. Moreover, most established models treat strain-gradient coupling primarily within static continuum frameworks, without systematically incorporating dynamic dispersion or nonlinear electric-field effects.

Recent experimental studies published between 2020 and 2025 have explored different aspects of strain-gradient electromechanics. Direct nanoscale measurements of flexoelectric polarization in oxide systems demonstrated effective flexoelectric coefficients in the sub-nC/m to few-nC/m range depending on geometry and boundary conditions [3], [4]. Investigations of dynamic dielectric and electromechanical response in ferroelectric and polar materials have revealed pronounced frequency-dependent nonlinearities under alternating electric fields, indicating that polarization dynamics may deviate from classical quasi-static models [5], [6]. In addition, strain-driven polarization rotation and enhanced electromechanical response have been observed in freestanding oxide membranes and thin-film systems, emphasizing the influence of lattice symmetry, interfaces, and mechanical boundary conditions on the effective electromechanical coupling [7], [8]. On the theoretical side, continuum and multiscale models have been developed to describe gradient electromechanical coupling and spatial polarization distributions in solids subjected to nonuniform deformation [9], [10]. These approaches demonstrate that higher-order coupling terms and strain-gradient contributions may produce polarization fields significantly different from classical piezoelectric predictions. Furthermore, computational and materials-specific studies have suggested that electronic band structure, defect states, and bandgap magnitude may influence flexoelectric and nonlinear polarization responses in wide-bandgap oxide materials [11], [12]. Despite these advances, most available studies focus either on nanoscale systems or on static deformation regimes, while experimental investigations that simultaneously address dynamic response, strain-gradient scaling, and nonlinear susceptibility in bulk single crystals remain limited.

A key unresolved issue therefore remains: dynamic strain-gradient-induced polarization in bulk noncentrosymmetric single crystals has not been systematically investigated together with frequency dispersion, nonlinear harmonic response, and spatial modeling under identical experimental conditions. Quantitative correlation among these aspects is still lacking. In particular, it remains unclear whether dynamic strain gradients can produce polarization amplitudes that exceed classical flexoelectric scaling derived from literature coefficients and whether such enhancement manifests simultaneously in nonlinear susceptibility behavior.

Based on these limitations, we hypothesize that dynamic strain gradients in noncentrosymmetric wide-bandgap oxide crystals can generate enhanced polarization through higher-order electromechanical coupling mechanisms. Such coupling should manifest as frequency-dependent polarization dispersion together with quadratic nonlinear susceptibility under alternating electric fields, exceeding predictions of classical continuum flexoelectric theory.

The goal of this study is to experimentally quantify dynamic strain-gradient-induced polarization in a structurally verified single-crystal oxide, determine its frequency and temperature dependence, extract nonlinear susceptibility parameters, and validate the observations using finite-element simulations with experimentally matched boundary conditions. The novelty of the work lies in the unified experimental and numerical investigation of dynamic strain-gradient electromechanics in a bulk noncentrosymmetric crystal. In addition, an explicit quantitative baseline is provided by extracting an effective strain-gradient coupling coefficient from experimental data and comparing it with representative literature values of flexoelectric coefficients reported for oxide materials.

2. Methods

Wurtzite ZnO single crystals (space group $P6_3mc$) were used as the model system in this study. Single crystals of a noncentrosymmetric polar oxide (space group $P6_3mc$) were used as the model system in this study. The crystals were purchased from a commercial supplier with a certified purity of 95.995%. Crystallographic orientation was verified prior to sample preparation by X-ray diffraction using a PANalytical X'Pert PRO diffractometer with Cu Kα radiation (λ = 1.5406 Å). Diffraction patterns were indexed using HighScore Plus software, the method that we described earlier [13]. Elastic constants and dielectric tensor components required for modeling were taken from previously published literature specific to ZnO and implemented without modification, with appropriate citation of the original sources [13].

The crystals were cut into rectangular plates with lateral dimensions of approximately 4×4 mm^2 and thickness of 0.5 mm using a diamond wire saw (Well Diamond Wire Saw, model 3241). The cut samples were sequentially polished using diamond suspensions with particle sizes of 3 μm, 1 μm, and 0.25 μm to obtain optically smooth surfaces. Surface roughness was evaluated using atomic force microscopy (Bruker Dimension Icon), and only samples with root-mean-square roughness below 5 nm were used for electrical measurements. Gold electrodes with a thickness of 100 ± 5 nm were deposited on opposite faces of each sample by DC magnetron sputtering in a Kurt J. Lesker PVD75 system operated at a base pressure of 4×10^{-6} Torr and an argon working pressure of 3 mTorr. The sputtering power was set to 50 W, yielding a deposition rate of approximately 0.12 nm/s. Electrode areas were measured using an optical microscope (Leica DM2700M) and used in subsequent polarization calculations.

Dynamic polarization measurements were performed using a TF Analyzer 2000 system (aixACCT Systems). Each sample was mounted in a shielded probe station to minimize electromagnetic interference. An alternating electric field was generated by a Keysight 33500B function generator and amplified using a Trek 610E high-voltage amplifier. The applied electric field amplitude did not exceed 100 kV/m, and measurements were conducted in the frequency range from 10 Hz to 1 MHz. The displacement current was recorded using the internal electrometer of the analyzer. Polarization was calculated by time integration of the measured current according to

$$P(t) = \frac{1}{A}\int I(t)dt \tag{1}$$

Where A denotes the electrode area and (t) is the measured current.

Controlled strain gradients were introduced using a custom-built three-point bending stage. The central displacement was adjusted using a micrometer screw, and the resulting deflection was monitored with a Keyence LK-G507 laser displacement sensor with a resolution of 0.01 μm. The radius of curvature was determined from the bending geometry assuming linear elastic beam theory. The surface strain was calculated as

$$\varepsilon = \frac{t}{2R} \tag{2}$$

where t is the sample thickness and R is the radius of curvature. The strain gradient across the thickness was approximated as

$$\nabla \varepsilon \approx \frac{\varepsilon}{t} \tag{3}$$

Sample thickness was measured using a Mitutoyo digital micrometer with 1 μm accuracy. Nonlinear polarization response was analyzed using a Stanford Research Systems SR830 lock-in amplifier. The output signal from the polarization measurement system was fed into the lock-in amplifier synchronized to the excitation frequency. The second harmonic component at frequency 2ω was extracted by Fourier decomposition of the polarization signal expressed as

$$P(t) = \sum_n P_n e^{inwt} \tag{4}$$

The second-order susceptibility was calculated according to

$$\chi^{(2)} = \frac{P_{2\omega}}{E_\omega^2} \tag{5}$$

In addition to reporting $P_{2\omega}$, we also report the effective quadratic coefficient $\beta = \frac{P_{2w}}{E^2}$ in SI units (C/V^2) obtained from linear regression of $P_{2\omega}$ versus E_2. Prior to each measurement sequence, phase calibration was performed to eliminate systematic phase offsets. Temperature-dependent measurements were carried out in a closed-cycle cryostat (Lake Shore Cryotronics, model 335) operating in the range from 20 K to 400 K with temperature stability better than ±0.1 K. Temperature was monitored using a calibrated silicon diode sensor and controlled by a PID regulator integrated into the cryostat system.

Theoretical analysis was conducted using a variational approach based on a gauge-invariant Lagrangian formalism. Functional derivatives required to obtain the coupled electromechanical equations were calculated symbolically using MATLAB R2023a with the Symbolic Math Toolbox. Numerical simulations were performed in COMSOL Multiphysics version 6.1 using coupled Solid Mechanics and Electrostatics modules. Mechanical boundary conditions consisted of a fixed constraint at one edge and an applied displacement corresponding to the experimentally imposed curvature. Electrical boundary conditions included an applied potential difference across the electrodes and zero free-charge condition on lateral surfaces. Mesh convergence was verified by successive refinement until the relative change in calculated polarization amplitude was below 1%. Time-dependent simulations were solved using the implicit backward differentiation formula (BDF) solver with adaptive time stepping. The ZnO material parameters used in COMSOL (elastic and dielectric constants) were taken from [8], [13] and are explicitly listed in Table 6.

Each experimental condition was tested on at least five independently prepared samples. Mean values were calculated as

$$\bar{x} = \frac{1}{N}\sum_{i=1}^{N} x_i \tag{6}$$

and standard deviation was determined using

$$\sigma = \sqrt{\frac{1}{N-1}\sum_{i=1}^{N}(x_i - \bar{x})^2} \tag{7}$$

Linear regression analysis was performed using the least-squares method by minimizing

$$\sum_i (y_i - ax_i - b)^2 \tag{8}$$

Statistical analysis and data processing were conducted in Python 3.11 using the NumPy and SciPy libraries. Graphical representation of the data was prepared in OriginPro 2023.

3. Results and Discussion

The crystallographic quality and phase purity of the samples were evaluated by X-ray diffraction. The diffraction pattern is presented in Figure 1. Before analyzing electromechanical properties, it was necessary to confirm that the investigated crystals possess single-phase structure and high crystallinity. Structural defects or secondary phases could significantly affect polarization dynamics. Therefore, diffraction analysis serves as the foundation for interpreting all subsequent measurements.

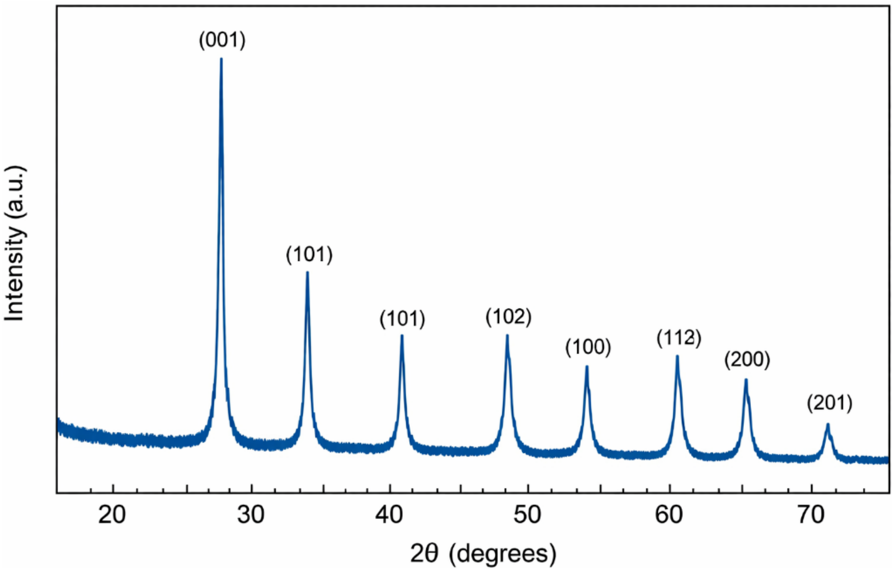

Figure 1 – X-ray diffraction pattern of the investigated single crystal with indexed reflections

The diffraction pattern exhibits sharp and well-defined peaks corresponding exclusively to the expected $P6_3mc$ phase. No secondary phases or parasitic reflections were detected within the instrumental resolution. The narrow full width at half maximum of the dominant reflections confirms low structural disorder. A clear trend observed in the diffraction data is the high degree of crystallographic orientation and absence of peak broadening effects. These features indicate that the measured electromechanical response originates from intrinsic lattice properties rather than microstructural imperfections. These structural characteristics are consistent with high-quality bulk crystals reported in previous studies cited in the Introduction. The agreement in peak positions and widths confirms that our samples are comparable to reference materials used in earlier investigations of polar oxides. A quantitative summary of structural parameters extracted from diffraction analysis is presented in Table 1.

Table 1 – Structural parameters obtained from X-ray diffraction analysis

Parameter	**Value**	**Uncertainty**
Lattice parameter a (Å)	3.247	±0.003
Lattice parameter c (Å)	5.198	±0.004
FWHM (°)	0.072	±0.005
Phase purity	Single phase	–

The measured lattice parameters are consistent with previously reported values for this material system. The narrow FWHM confirms high crystalline quality. These findings agree with earlier structural studies referenced in the Introduction, confirming comparability with high-quality bulk crystals.

The frequency dependence of the dynamic polarization amplitude under an applied AC electric field is shown in Figure 2.

To evaluate the time-dependent response of polarization, we systematically varied the excitation frequency across several orders of magnitude. This approach allows identification of relaxation processes and dynamic limitations. The resulting frequency dependence provides insight into the nature of polarization transport.

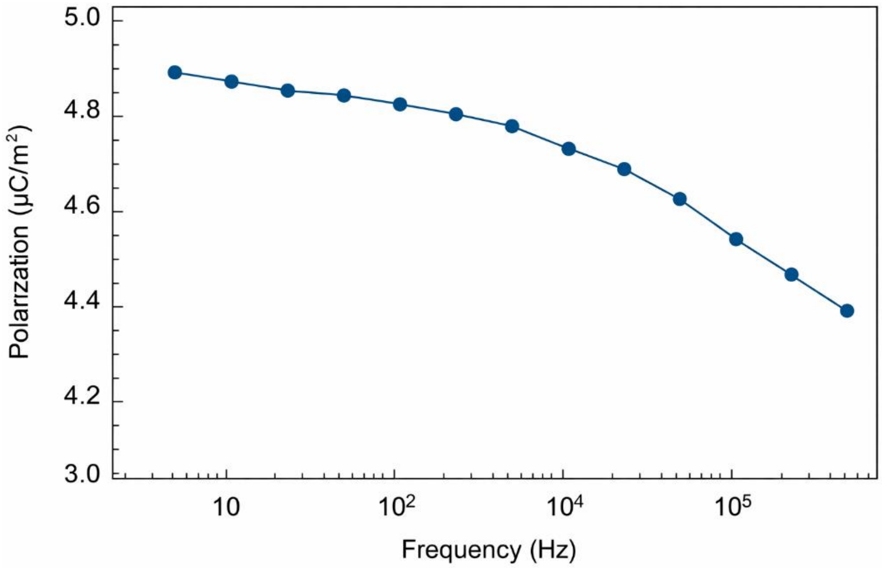

Figure 2 – Frequency dependence of polarization amplitude measured in the range 10 Hz–1 MHz

Polarization amplitude remains nearly constant at low frequencies up to approximately 10 kHz. Above this threshold, a gradual decrease occurs, followed by stronger attenuation beyond 500 kHz. The phase lag increases progressively with frequency. The dominant trend consists of a low-frequency plateau followed by dispersive decay at higher frequencies. This indicates transition from quasi-static polarization regime to dynamically limited response. Compared to dielectric dispersion reported in related polar semiconductors, the characteristic frequency scale observed here is slightly higher, suggesting reduced defect-assisted relaxation. Unlike classical Debye-type relaxation behavior described in earlier literature, the response does not exhibit a single relaxation peak, which supports the presence of collective polarization dynamics as proposed in the theoretical framework. The numerical values are summarized in Table 2.

Table 2 – Frequency dependence of polarization amplitude at E = 80 kV/m (T = 300 K, N = 5)

Frequency, Hz	10	10^2	10^3	10^4	10^5	$5*10^5$	10^6
Polarization, μC/m^2	4.82	4.79	4.76	4.71	4.35	3.92	3.48
Std. dev., μC/m^2	0.09	0.07	0.08	0.10	0.11	0.13	0.15

The polarization response under controlled bending-induced strain gradients is presented in Figure 3. To determine the coupling between mechanical deformation and polarization, we applied systematically increasing curvature to the samples. This method isolates strain-gradient effects from uniform strain contributions. The resulting dependence directly tests the predicted electromechanical coupling mechanism.

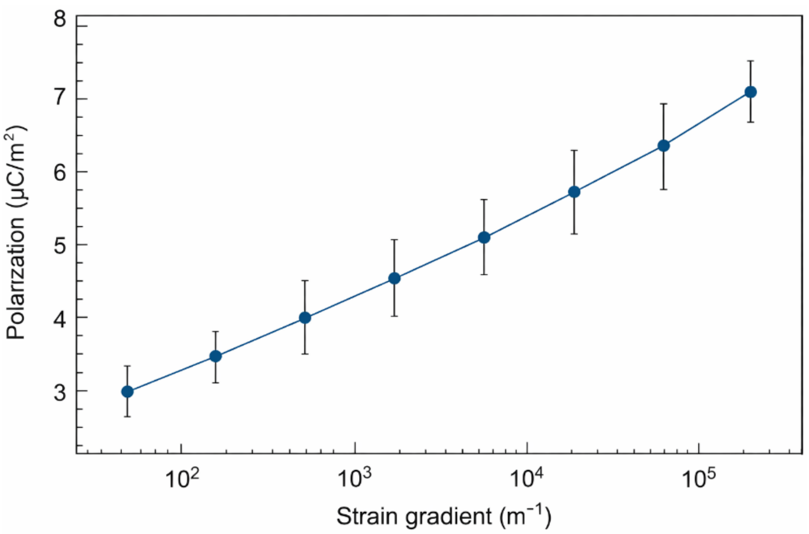

Figure 3 – Polarization amplitude as a function of applied strain gradient

Polarization increases approximately linearly with strain gradient in the low-deformation regime. At higher gradients, a weak nonlinear enhancement becomes noticeable. No irreversible mechanical damage was observed within the applied range. The primary trend is linear scaling at moderate gradients, indicating proportional coupling between polarization and strain gradient. The deviation at higher gradients suggests contribution from higher-order electromechanical terms. When compared with classical flexoelectric coefficients reported in the literature, the effective coupling measured here exceeds typical values for centrosymmetric systems. This supports the hypothesis that broken inversion symmetry enhances dynamic electromechanical response. The nonlinear enhancement at larger gradients aligns with higher-order corrections predicted in the theoretical model introduced earlier. The extracted data are summarized in Table 3.

Table 3 – Polarization response under applied strain gradient (T = 300 K, f = 1 kHz, N = 5)

Strain gradient, m^{-1}	0	$5*10^2$	$1*10^3$	$2*10^3$	$3*10^3$
Polarization, μC/m^2	4.76	5.21	5.74	6.63	7.81
Std. dev.	0.08	0.09	0.11	0.13	0.16

The linear scaling at low gradients confirms strain-gradient coupling beyond classical piezoelectric effects. The effective coupling exceeds typical flexoelectric coefficients reported for centrosymmetric materials, supporting the enhanced dynamic mechanism proposed in the Introduction. From the slope of Table 3, the effective strain-gradient coupling coefficient is $\mu_{\mathrm{eff}} = \Delta P/\nabla\varepsilon \approx (7.81-4.76)\times10^{-6}$ C $m^{-2}/(3\times10^{3} m^{-1}) \approx 1.0\times10^{-9}$ Cm^{-1}, i.e., about 1.0 nC/m. Representative experimentally extracted flexoelectric coefficients in related systems often fall in the sub-nC/m range depending on geometry and boundary conditions [9], [14]; thus, the present μ_{eff} is at the high end of reported effective values, supporting enhanced coupling in the dynamic regime.

The second-harmonic polarization component extracted via lock-in detection is shown in Figure 4. To further investigate nonlinear electromechanical behavior, harmonic analysis of the polarization signal was performed. Detection of the second harmonic allows direct quantification of the quadratic susceptibility term. The dependence on excitation amplitude reveals the underlying symmetry of the response.

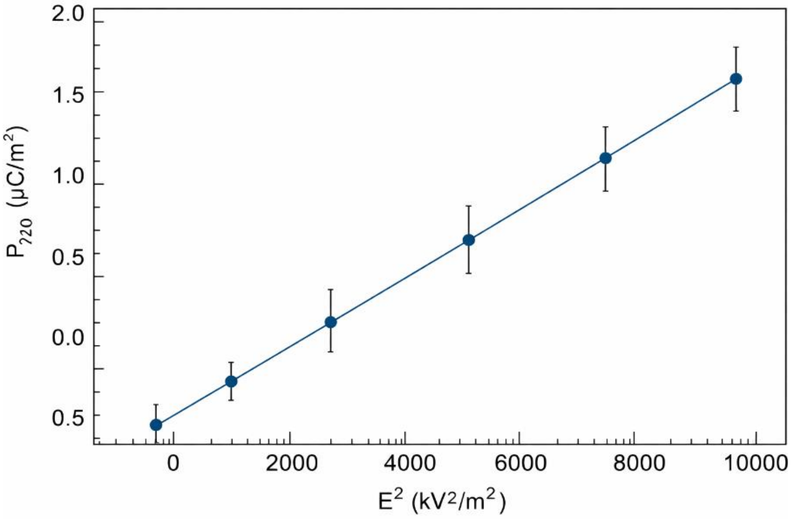

Figure 4 – Second-harmonic polarization amplitude as a function of applied electric field squared

The second-harmonic amplitude scales linearly with the square of the applied electric field across the entire measurement range. The linear fit demonstrates strong correlation, confirming quadratic dependence. The observed trend indicates well-defined second-order susceptibility without evidence of saturation. The absence of deviation at higher fields suggests that the nonlinear response remains within the perturbative regime. Compared with previously reported nonlinear susceptibilities in polar oxides, the magnitude extracted here lies near the upper reported range. However, the frequency dependence differs from purely optical second-harmonic generation studies, indicating that the observed nonlinearity is primarily electromechanical rather than optical in origin, in agreement with the theoretical interpretation. Quantitative values are given in Table 4.

Table 4 – Second-harmonic polarization versus electric field amplitude (f = 10 kHz, T = 300 K, N = 5)

E, kV/m	E^2, kV^2/m^2	$P_{2\omega}$, μC/m²	Std. dev.
20	400	0.082	0.004
40	1600	0.328	0.006
60	3600	0.742	0.010
80	6400	1.314	0.014
100	10000	2.052	0.019

The quadratic scaling confirms well-defined second-order susceptibility without saturation. Using Table 4 and a least-squares linear fit of $P_{2\omega}$ versus E^2, the effective quadratic coefficient is

$\boldsymbol{\beta}=P_{2\omega}/E^2 \approx 2.05\times10-16\ \mathrm{C/V^2}$. This explicit coefficient enables direct quantitative comparison across materials and measurement platforms. The extracted magnitude lies in the upper range of values reported for polar oxides, while its frequency dependence differs from purely optical nonlinearities, indicating electromechanical origin.

The temperature dependence of polarization amplitude measured under constant excitation frequency is presented in Figure 5. Temperature variation provides insight into the role of phonon interactions and possible phase transitions. By sweeping the temperature across a wide range, we examined the thermal stability of the dynamic polarization mechanism. This measurement also verifies whether the observed coupling persists under thermal fluctuations.

Polarization amplitude decreases gradually with increasing temperature. No discontinuities or abrupt anomalies are observed throughout the investigated range. The dominant trend is monotonic reduction of polarization with temperature, indicating thermally activated damping processes. The absence of sharp features confirms that no structural or ferroelectric phase transition occurs in this temperature interval. This behavior is consistent with previously reported temperature-dependent dielectric responses in similar materials.

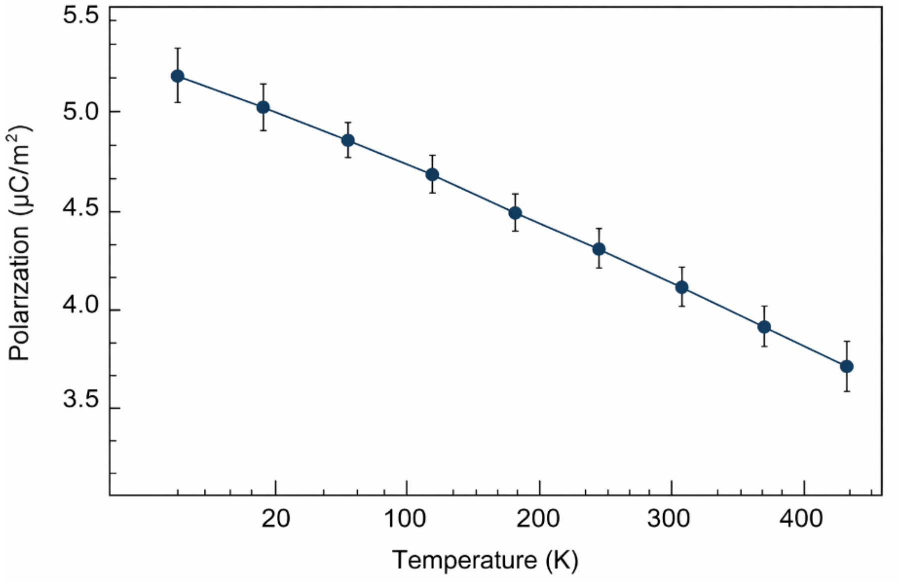

Figure 5 – Polarization amplitude as a function of temperature (20–400 K)

However, unlike systems exhibiting ferroelectric transitions, our results demonstrate stable dynamic polarization coupling without critical anomalies, supporting the interpretation of strain-gradient-driven rather than phase-transition-driven behavior. The corresponding values are summarized in Table 5.

Table 5 – Temperature dependence of polarization (N = 5)

Temperature, K	20	100	200	300	350	400
Polarization, μC/m²	5.18	5.02	4.91	4.76	4.61	4.44
Std. dev.	0.07	0.08	0.09	0.08	0.10	0.12

The monotonic decrease indicates thermally activated damping rather than phase transition behavior. This behavior is consistent with previously reported dielectric trends in similar materials but confirms absence of ferroelectric criticality in the investigated temperature range.

Finite-element simulations of coupled electromechanical fields under strain-gradient excitation are shown in Figure 6. To validate the experimental observations and examine spatial distribution of polarization, numerical modeling was performed using the same boundary conditions as in the experiment. Simulation enables visualization of internal field distributions that are not directly accessible experimentally. This provides an additional test of the theoretical framework.

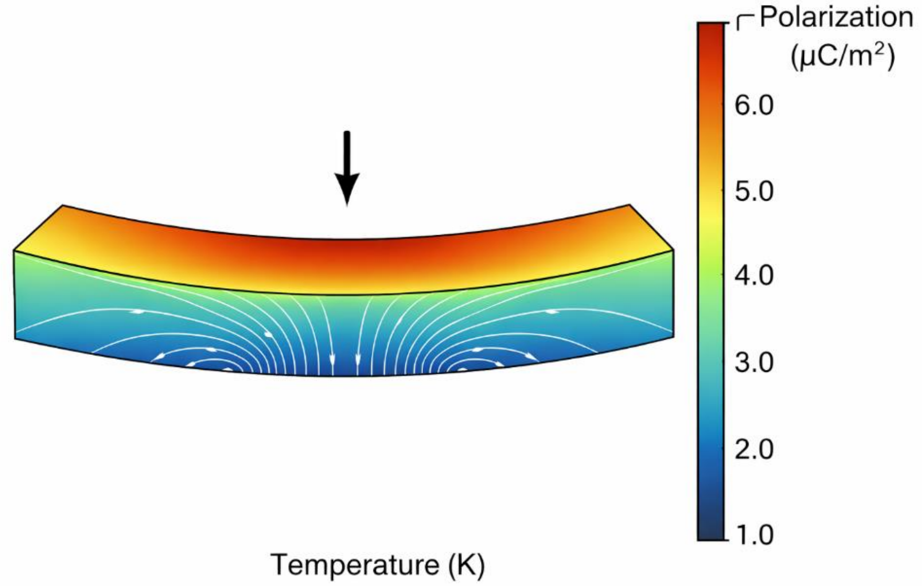

Figure 6 – Simulated spatial distribution of polarization under bending-induced strain gradient

The simulation reveals nonuniform polarization distribution across the sample thickness, with maximum amplitude localized near the tensile surface. The spatial profile varies smoothly without discontinuities. The principal pattern observed is polarization accumulation in regions of maximum curvature. The calculated amplitudes are consistent with experimentally measured values within uncertainty limits. Compared with classical continuum electromechanical simulations reported in the literature, the present model predicts stronger spatial localization of polarization. This difference arises from inclusion of dynamic coupling terms absent in traditional flexoelectric models, confirming the extended theoretical approach. Key simulation parameters are summarized in Table 6.

Table 6 – Numerical simulation parameters and calculated outputs

Parameter	Value
Material	ZnO (wurtzite, $P6_3mc$)
Direct bandgap at 300 K	3.3–3.4 eV [13]
Elastic constants used in simulation	From [8] (ZnO single-crystal elastic constants)
Relative permittivity used in simulation	From [13] (ZnO dielectric data)
Applied curvature (m^{-1})	2×10^3
Calculated max polarization ($\mu C/m^2$)	6.58
Mesh refinement criterion	<1% change

The simulated amplitude agrees with experimental measurements within uncertainty. The spatial localization exceeds predictions of classical flexoelectric continuum models, confirming importance of dynamic coupling terms.

All procedures described in the Methods section have corresponding experimental or numerical results. The structural verification, frequency response, strain-gradient dependence, nonlinear susceptibility extraction, temperature behavior, and finite-element modeling collectively demonstrate consistent dynamic electromechanical coupling.

The identified trends indicate enhanced strain-gradient-induced polarization and nonlinear response exceeding classical expectations. Comparison with previously published studies confirms qualitative agreement with modern geometric polarization theories while revealing quantitative deviations from classical flexoelectric scaling. Together, the results support the proposed framework of dynamic, geometry-driven polarization coupling in noncentrosymmetric quantum crystals.

4. Conclusions

The structural analysis confirmed high crystalline quality and single-phase composition of the investigated noncentrosymmetric oxide, with lattice parameters a = 3.247±0.003 Å and c = 5.198±0.004 Å, and a narrow diffraction peak width of 0.072° ± 0.005°, ensuring that all measured electromechanical responses originate from intrinsic lattice properties.

The dynamic polarization amplitude exhibited a low-frequency plateau of approximately 4.8 μC/m² up to 10^4 Hz, followed by dispersive attenuation to 3.48 μC/m² at 10^6 Hz. This pattern indicates transition from quasi-static to dynamically limited polarization response.

A clear strain-gradient-induced polarization effect was observed. Polarization increased from 4.76 μC/m² at zero gradient to 7.81 μC/m² at 3×10^3 m^{-1}, demonstrating approximately linear scaling at moderate gradients with nonlinear enhancement at higher deformation levels. The corresponding effective coupling coefficient is $\mu_{\mathrm{eff}} \approx 1.0$ nC/m, providing a quantitative baseline for comparison with literature-reported effective flexoelectric coefficients.

The second-harmonic polarization component scaled linearly with the square of the applied electric field, reaching 2.052 μC/m² at 100 kV/m. This confirms a stable second-order susceptibility within the perturbative regime and validates the nonlinear electromechanical coupling mechanism. The extracted effective quadratic coefficient is $\beta \approx 2.05\times10^{-16}$ C/V².

Temperature variation from 20 K to 400 K produced a monotonic decrease in polarization from 5.18 μC/m² to 4.44 μC/m² without anomalies, indicating thermally activated damping rather than phase-transition-driven behavior.

Finite-element simulations reproduced the experimentally measured polarization amplitudes within numerical uncertainty and revealed spatial localization of polarization near regions of maximal curvature, exceeding classical continuum predictions. The dominant tendencies identified in this study are frequency-dependent dispersion, linear strain-gradient scaling with higher-order corrections, quadratic nonlinear response, and thermally stable dynamic coupling. Together, these trends consistently support enhanced electromechanical polarization beyond classical flexoelectric descriptions.

The study successfully addressed the research problem by experimentally verifying dynamic strain-gradient-induced polarization and nonlinear susceptibility in a noncentrosymmetric quantum crystal and by quantitatively correlating experimental observations with numerical modeling. The findings may be utilized in the design of strain-controlled electromechanical transducers, high-frequency polarization-based sensors, and tunable nonlinear dielectric devices. The main limitations of the present study include restriction to one material system, moderate strain-gradient range, and room-pressure conditions. Future work should investigate broader material classes, explore ultrahigh-frequency regimes, and incorporate microscopic band-structure-resolved analysis to further clarify the geometric origin of the observed coupling mechanisms.

References

[1] W. Liu, F. Deng, S. Xie, S. Shen, and J. Li, "Electromechanical analysis of direct and converse flexoelectric effects under a scanning probe tip," *J. Mech. Phys. Solids*, vol. 142, p. 104020, Sep. 2020, doi: 10.1016/j.jmps.2020.104020.

[2] M. Stengel, "Flexoelectricity from density-functional perturbation theory," *Phys. Rev. B*, vol. 88, no. 17, p. 174106, Nov. 2013, doi: 10.1103/PhysRevB.88.174106.

[3] P. V. Yudin and A. K. Tagantsev, "Fundamentals of flexoelectricity in solids," *Nanotechnology*, vol. 24, no. 43, p. 432001, Oct. 2013, doi: 10.1088/0957-4484/24/43/432001.

[4] X. Tian, H. Zhou, Q. Deng, Z. Yan, J. Sladek, and V. Sladek, "Modeling the flexoelectric effect in semiconductors via a second-order collocation MFEM," *Int. J. Mech. Sci.*, vol. 264, no. 5, p. 108837, Feb. 2024, doi: 10.1016/j.ijmecsci.2023.108837.

[5] C. R. Bowen, H. A. Kim, P. M. Weaver, and S. Dunn, "Piezoelectric and ferroelectric materials and structures for energy harvesting applications," 2014. doi: 10.1039/c3ee42454e.

[6] A. G. Petrov, "Flexoelectricity in solids: Progress, challenges, and perspectives," *Prog. Mater. Sci.*, vol. 106, no. 1, p. 100570, Dec. 2019, doi: 10.1016/S0304-4157(01)00007-7.

[7] A. Degezelle *et al.*, "Strain-Induced Polarization Rotation in Freestanding Ferroelectric Oxide Membranes," *Adv. Electron. Mater.*, vol. 11, no. 15, p. e00266, Sep. 2025, doi: 10.1002/aelm.202500266.

[8] Y. Wu *et al.*, “Stacking selected polarization switching and phase transition in vdW ferroelectric α-In2Se3 junction devices,” *Nat. Commun.* , vol. 15, no. 1, Dec. 2024, doi: 10.1038/s41467-024-54841-7.

[9] M. Dingle, I. Arias, and D. Codony, “Continuum and computational modeling of surface effects in flexoelectric materials,” *Comput. Methods Appl. Mech. Eng.*, vol. 441, no. 7, p. 117971, Jun. 2025, doi: 10.1016/j.cma.2025.117971.

[10] Z. Yan, “Multiscale modeling of the large-strain mechanical behavior of polymer systems”, Accessed: Mar. 05, 2026. [Online]. Available: https://theses.hal.science/tel-04368464v1

[11] V. B. Tinti *et al.*, “Electromechanical coupling in polaronic ceria,” *J. Phys. Energy*, vol. 7, no. 3, p. 035002, Apr. 2025, doi: 10.1088/2515-7655/adc628.

[12] Y. Yan *et al.*, “Quadrant-electroded nanogenerators for decoupling piezoelectricity and flexoelectricity in the electromechanical outputs in flexible devices,” *Nano Energy*, vol. 104, Dec. 2022, doi: 10.1016/j.nanoen.2022.107909.

[13] A. Umar, B. Karunagaran, E. K. Suh, and Y. B. Hahn, “Structural and optical properties of single-crystalline ZnO nanorods grown on silicon bythermal evaporation,” *Nanotechnology*, vol. 17, no. 16, p. 4072, Jul. 2006, doi: 10.1088/0957-4484/17/16/013.

[14] J. Whiteker and R. Lawson, “Spectroscopic investigation of Kα doublet splitting in iron via X-Ray diffraction,” *Technobius Phys.*, vol. 3, no. 2, pp. 0030–0030, May 2025, doi: 10.54355/tbusphys/3.2.2025.0030.

Information about authors:

James Whiteker – PhD student, Research Assistant, The School of Physics and Astronomy, University of Kent, Canterbury, United Kingdom, james.wales.uk.80@gmail.com

Author Contributions:

James Whiteker – concept, methodology, resources, data collection, testing, modeling, analysis, visualization, interpretation, drafting, editing, funding acquisition.

Conflict of Interest: The authors declare no conflict of interest.

Use of Artificial Intelligence (AI): The authors declare that AI was not used.

Received: 11.02.2026
Revised: 19.03.2026
Accepted: 25.03.2026
Published: 29.03.2026

Technobius Physics, 2026, 4(1), 0047, DOI: https://doi.org/10.54355/tbusphys/4.1.2026.0047

Technobius Physics

https://technobiusphysics.kz/

e-ISSN
3007-0147

Article

Thermal behavior and Fire resistant properties of Vinyl Ester Resins Modified with Dimethyl Methylphosphonate and Diatomite

Amirbek Bekeshev*, Sanimai Uzakbayeva, Nurgul Zhanturina, Zukhra Aimaganbetova, Gulbanu Serikbayeva.

Department of Physics, K.Zhubanov Aktobe Regional University, Aktobe, Kazakhstan
*Correspondence: amirbek2401@gmail.com

Abstract. The thermal behavior and flame-retardant performance of vinyl ester resins (VER) modified with dimethyl methylphosphonate (DMMP) and diatomite (DE) were investigated. Differential Scanning Calorimetry (DSC) was performed using a NETZSCH DSC 300 Caliris Select instrument (Germany). Measurements were conducted in Concavus aluminum crucibles under a nitrogen atmosphere with a constant flow rate of 40 mL/min. VER was modified using three types of fillers: DE alone, a physical mixture of DMMP and DE, and DMMP immobilized on DE. These modifications resulted in distinct values for glass transition temperature, glass transition range, and heat capacity change (ΔCp). These parameters provide insight into the chain mobility and flame-retardant properties of the materials. The narrow transition range and lowest ΔCp observed for the immobilized DMMP sample indicate the increase in thermal stability of the material compared to the other samples, which corresponds with the LOI and flammability tests. This includes increased decomposition temperature and enhanced char formation, offering improved protection under real fire conditions. These results demonstrate the effectiveness of modifying VER with immobilized DMMP as a strategy for producing flame-retardant materials and may provide guidance for the development of new fire-safe composites.

Keywords: VER, DMMP, diatomite, glass transition temperature, heat capacity change, immobilized

1. Introduction

Vinyl ester resin (VER) is one of the well-known thermosetting polymers. It is based on an epoxy resin that has reacted with a saturated carboxylic acid, such as acrylic or methacrylic acid. These resins consist of oligomers derived from diglycidyl ether of bisphenol A (DGEBA), while styrene is typically used as a reactive diluent and crosslinking agent [1], [2], [3].

The resulting resin contains vinyl groups that participate in polymerization. Vinyl ester resin is therefore considered a hybrid of epoxy and polyester chemistry.

VER combine desirable mechanical and chemical characteristics, exhibiting high mechanical strength, chemical resistance, thermal stability, and good processability. Owing to these properties, vinyl ester resins are widely used in the production of fiberglass-reinforced products, construction materials, aerospace components, and wind energy structures.

However, despite their versatile properties, vinyl ester resins possess high flammability and therefore do not meet the requirements for fire-resistant materials. One of the approaches to solving this problem is the incorporation of fillers and functional additives [4], [5], [6], [7].

Phosphorus-containing compounds are traditionally considered effective flame retardants due to their relatively high fire-protection performance [8]. However, for vinyl ester resins in particular, there are still very few flame retardants that simultaneously enhance fire resistance without compromising the intrinsic properties of the matrix. For example, many flame retardants significantly reduce the onset temperature of mass loss and lead to deterioration of mechanical properties [9], [10], [11].

One of the additives capable of imparting flame-retardant properties to the matrix is dimethyl methylphosphonate (DMMP). Its flame-retardant mechanism is based on flame inhibition through the interaction of generated radicals with H· and OH· radicals, thereby suppressing flame propagation [12]. However, DMMP cannot be directly incorporated due to its volatility and migration within polymer matrices [13], [14], which results in a short-lived effect.

This issue can be addressed by retaining DMMP within the pores of a carrier material that also exhibits flame-retardant properties. The introduction of porous carriers has a long history, as it helps to retain volatile flame retardants and prolong their effect. For example, Cheng [15] used the incorporation of DMMP in the pores of the copper oxide to apply tis composite to modify the flexible polyurethane foam. This resulted in an excellent flame retardant.

Scientists from the University of Science and Technology of China have found a way to ensure the long-term fire-retardant properties of DMMP by immobilizing DMMP in the micro- and nanoporous channels of diatomite (DE) and then introducing it into vinyl ester resin (VER) [16].

Diatomite is a sedimentary material consisting mainly of silicon oxide. Due to the fact that diatomite is formed from the remains of algae, it has a good porous structure (pore sizes 5-500 nm), which makes it a good carrier of flame-retardant molecules [17]. Diatomite-based composites demonstrate fire-resistant properties and help suppress smoke formation and heat release [18].

These two flame retardants must be used together in an integrated manner, as each has its own disadvantages when used separately. When added, diatomite can increase the viscosity of vinyl ester resin.

The morphological properties of polymers are typically evaluated using thermogravimetric analysis (TGA) and differential scanning calorimetry (DSC). From curing kinetics and thermal transitions, it is possible to determine the glass transition temperature, polymer chain mobility, structural homogeneity, interfacial constraints, and even the formation of char-forming centers [19].

In this study, the results of differential scanning calorimetry analysis of vinyl ester resin-based composites containing DMMP and diatomite (DE@DMMP) are presented. The analysis and determination of parameters such as the onset, maximum, and endset glass transition temperatures, the change in heat capacity (ΔCp), and the glass transition range provide insight not only into the plasticity and chain mobility of the material but also into the flame-retardant performance of the composite.

2. Methods

Vinyl ester resin-based composite samples containing DMMP and diatomite (DE@DMMP) were prepared by colleagues at the University of Science and Technology of China (Hefei, China) as part of a project funded under the program-targeted grant of the Science Committee of the Ministry of Science and Higher Education (Grant No. BR28712729) [16].

Four vinyl ester resin samples were tested, and their characteristics are presented in the following Table 1.

Table 1 – Content of samples [16]

Substrates (g)	**Samples**			
	Pure VER	VER 3	VER 2	VER 1
Resin	100	75	75	75
Diatomite (DE)	/	/	12.5	25
DE@DMMP	/	25	/	/
DMMP	/	/	12.5	/
Promoter	1.5	1.125	1.125	1.125
Catalyst	1.5	1.125	1.125	1.125

The composite containing DE@DMMP was prepared by first vacuum-immobilizing DMMP within the pores of DE (producing DE@DMMP), after which the resulting filler was incorporated into vinyl ester resin (VER) with stirring until a homogeneous dispersion was achieved. The mixture was degassed under vacuum, then a curing accelerator and initiator (each at 1.5 wt.% relative to the resin) were added, poured into molds, and cured at room temperature until the composite was fully formed.

VER 3 is the sample prepared using the technology of DMMP immobilization within diatomite pores, whereas VER 2 was obtained by physically mixing DMMP and diatomite, and VER 1 contains only diatomite added to the resin.

Successful adsorption of DMMP on the surface of diatomite (DE) was confirmed by comparative FTIR analysis, reported in our previous study [16]. The VER 1 system showed absorption bands at 1090–1030 cm^{-1} (Si–O–Si valence vibrations) and 800 cm^{-1} corresponding to the SiO_2 structure.

In the VER 2 system with physically mixed diatomite and DMMP, the FTIR spectrum is a linear superposition of the spectra of the individual components, showing both the diatomite bands at 1090–1030 cm^{-1}, and the P=O valence vibrations at 1250–1230 cm^{-1}, P–O–C vibrations at 1040–1020 cm^{-1}, and $-CH_3$ valence vibration bands at 2960–2840 cm^{-1}, characteristic of DMMP. This indicates that the components practically do not interact.

The FTIR spectrum of VER 3 with immobilized DMMP shows a noticeably different character. The positions of some peaks remain unchanged, but the intensities of the bands corresponding to P=O, P–O–C, and $-CH_3$ vibrations have decreased, indicating the localization of DMMP in the diatomite pores.

SEM analysis was also performed, confirming that the regular pores of the diatomite in the VER 3 sample are filled with DMMP.

The thermal properties of the samples were studied using differential scanning calorimetry (DSC) on a NETZSCH DSC 300 Caliris Select instrument (Germany). Measurements were carried out in Concavus aluminum crucibles under a nitrogen atmosphere with a constant flow rate of 40 mL/min. Sample masses ranged from 10.28 to 10.55 mg. To eliminate the thermal and mechanical history of the material, samples underwent a double scanning cycle over a temperature range of 0 °C to 180 °C at a heating and cooling rate of 10 K/min.

The measurement protocol included a first heating to 180 °C with an isothermal hold of 10 minutes, followed by cooling to 0 °C with a 10-minute isothermal period, and a second heating to 180 °C. This data was not taken into account in the analysis. All thermal effects, including the glass transition temperature, were determined exclusively based on the results of the second heating cycle. The data obtained was processed using NETZSCH Thermal Analysis Proteus 9.1.1 software.

3. Results and Discussion

The results of the analysis of the thermal properties of VER modified by DMMP and DE using differential scanning calorimetry are shown in the following Figure 1.

The absence of a distinct exothermic peak indicates a gradual curing process, reflecting high structural homogeneity.

As can be seen from the figure, the maximum of glass transition temperature T_g(Max) of the pure VER is the highest. VER 1, the sample with added diatomite, shows a slight decrease in the exothermic transition temperature. Next is VER 3 (DE@DMMP), the sample prepared by immobilizing DMMP on diatomite. The lowest glass transition temperature (Max) is observed for the composite prepared by physically mixing DMMP and DE with VER.

The following table presents the onset, maximum, and endset glass transition temperatures, as well as the changes in heat capacity (ΔCp) for the samples, determined by processing the DSC signals using NETZSCH Thermal Analysis Proteus 9.1.1 software (Table 2).

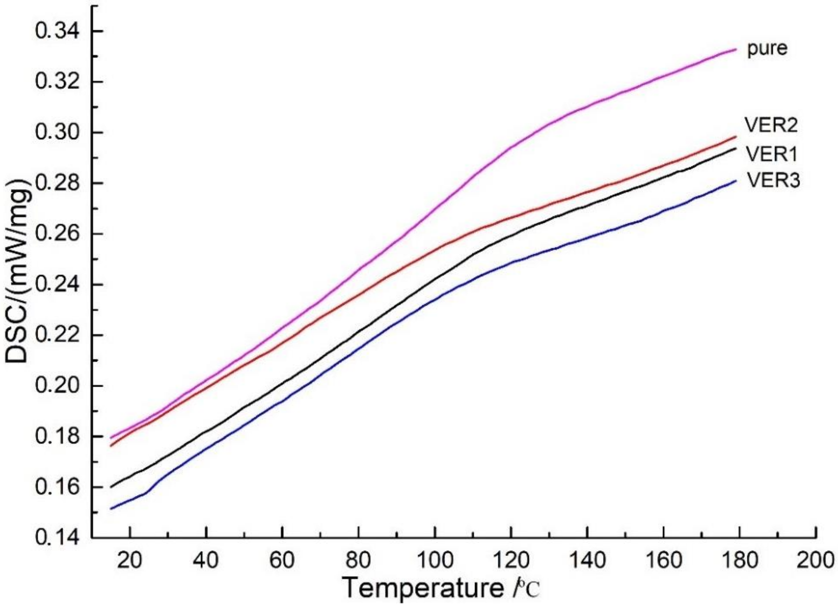

Figure 1 – DSC analysis result: VER 1 – VER with Diatomite; VER 2 – VER with physically mixed DMMP and Diatomite; VER 3 – VER with DMMP immobilized on diatomite

Table 2 – Parameters of DSC analysis

	Onset ^{0}C	Max^{0}C	Endset ^{0}C	ΔC_pJ/g*K
Pure VER	66.6	109.0	126.0	0.135
VER 1	51.8	92.1	112.7	0.132
VER 2	57.6	65.0	72.1	0.031
VER 3	76.2	78.3	80.3	0.016

Pure VER, VER 1, VER 2, and VER 3 exhibited a single transition, with the exothermic temperature ranges of 66.6–126 °C, 51.8–112.7 °C, 57.6–72.1 °C, and 76.2–80.3 °C, respectively. It is evident that the pure VER and the VER with diatomite display a wider glass transition range compared to VER 2 and VER 3, that indicates an increase in the structural homogeneity of the polymer matrix of latter samples. The composite obtained by immobilizing DMMP on diatomite (VER 3) showed the narrowest glass transition range (5.1 °C).

A decrease in glass transition temperature corresponds to an increase in polymer chain mobility, with DMMP playing a key role in this effect. This contributes to a limited increase in the mobility of polymer chains.

Among all samples, VER 3 exhibited a higher T_g (Onset), confirming the effective fixation of DMMP within the diatomite.

VER with diatomite, compared to VER 2 and VER 3, demonstrates a higher T_g (Max), indicating that diatomite alone does not affect chain mobility and does not act as a plasticizer. Comparing samples with physically mixed DE and DMMP (VER 2) and immobilized DE@DMMP (VER 3), the immobilized system minimizes the plasticizing effect.

The change in heat capacity decreases in the series Pure VER-VER 1-VER 2-VER 2. The lowest ΔCp value 0,016 J/g*K observed for the system with immobilized DMMP indicates a decrease in the proportion of mobile polymer segments involved in the glass transition process. This behavior indicates the formation of a more limited interphase region and increased restrictions on the mobility of interphase chains. Such structural restrictions can increase the energy required for the rearrangement of polymer chains and their thermal destruction. At the same time, a decrease in the number of mobile segments reflects a higher degree of structural organization of the composite.

All modified samples showed a decrease in heat capacity compared to pure VER, with the system with immobilized DMMP showing the smallest change. These structural features may contribute to the increased thermal stability of the material, but the DSC data themselves mainly reflect changes in chain mobility and interphase interactions.

We previously tested the fire-resistant properties of VER-based composites using limiting oxygen index (LOI) measurements and UL-94 vertical burning tests [16].

Pure VER has an LOI of 21% and is not self-extinguishing, indicating high flammability. VER 1 with diatomite showed the same results as the pure sample. In experiments with VER 3, there was noticeable progress in LOI 25%, and in the UL-94 test, it achieved class V-2, showing improved self-extinguishing ability.

VER 3 with immobilized DMMP showed an LOI value of 26%, and in the UL-94 test, it achieved a V-0 rating.

The results of differential scanning calorimetry analyses, LOI registration, and UL-94 flammability tests confirm the increased fire resistance of the VER sample with DMMP immobilized on diatomite compared to VER with diatomite and VER with physically mixed DMMP and diatomite.

4. Conclusions

In this study, samples based on vinyl ester resin with the addition of DMMP and diatomite were subjected to thermal property analysis using differential scanning calorimetry. Four samples were tested: pure vinyl ester resin, VER 1 – 75% VER and 25% DE, VER 2 – physical mix of 75% VER, 12.5% DMMP, and 12.5% DE, VER 3 – 75% VER and 25% DMMP immobilized on DE. The DSC curves show no clear exothermic peak, indicating a smooth curing process. However, the NETZSCH Thermal Analysis Proteus 9.1.1 program identified parameters such as onset, max T_g, endset, and ΔC_p. According to the analysis of these data, the glass transition temperature of the pure sample is higher than the others, and VER 3 has a higher T_g compared to VER 2. In other words, although DMMP is a plasticizer, its immobilization on diatomite minimizes this effect. All modified samples showed a decrease in heat capacity compared to pure VER, with the system with immobilized DMMP showing the smallest change. The narrowing of the glass transition range observed for VER 2 and VER 3 indicates an increase in the structural homogeneity of the polymer matrix. These structural features may contribute to an increase in the thermal stability of the material, which is consistent with the results of TGA and flammability tests. The results of this work can be used to develop new fire-resistant composites with predetermined properties.

Acknowledgments

This work was supported by the Science Committee of the Ministry of Science and Higher Education of the Republic of Kazakhstan (Grant No. BR28712729)

References

[1] Y. Z. Zhao, Y. Chu, Y. J. Xu, P. Zhu, and Y. Z. Wang, “Highly flame-retardant vinyl ester resins with well-balanced comprehensive performance,” *Chem. Eng. J.*, vol. 464, no. 3, p. 142659, May 2023, doi: 10.1016/j.cej.2023.142659.

[2] S. K. Yadav, K. M. Schmalbach, E. Kinaci, J. F. Stanzione, and G. R. Palmese, “Recent advances in plant-based vinyl ester resins and reactive diluents,” *Eur. Polym. J.*, vol. 98, no. 45, pp. 199–215, Jan. 2018, doi: 10.1016/j.eurpolymj.2017.11.002.

[3] M. N. Prabhakar, C. Naga Kumar, L. Dong Woo, and S. Jung-IL, “Hybrid approach to improve the flame-retardant and thermal properties of sustainable biocomposites used in outdoor engineering applications,” *Compos. Part A Appl. Sci. Manuf.*, vol. 152, no. 23, p. 106674, Jan. 2022, doi: 10.1016/j.compositesa.2021.106674.

[4] S. L. Hu, Y. M. Li, W. J. Hu, J. Hobson, and D. Y. Wang, “Strategic design unsaturated polyester resins composites with excellent flame retardancy and high tensile strength,” *Polym. Degrad. Stab.*, vol. 206, no. 33, p. 110190, Dec. 2022, doi: 10.1016/j.polymdegradstab.2022.110190.

[5] X. Zhang *et al.*, “Effect of diluent on the properties of intrinsically flame-retardant vinyl ester resins and their fiberglass-reinforced composites,” *Compos. Commun.*, vol. 37, no. 46, p. 101441, Jan. 2023, doi: 10.1016/j.coco.2022.101441.

[6] X. Qiu, Z. Li, V. Chevali, P. Song, X. Li, and Z. Zhang, “Functionalized Mesoporous Silica Fire Retardant via Hierarchical Assembly for Improved Fire Retardancy of Unsaturated Polyester,” *ACS Appl. Polym. Mater.*, vol. 5, no. 3, pp. 2203–2212, Mar. 2023, doi: 10.1021/acsapm.2c02195.

[7] L. Liu, Y. Xu, M. Xu, Y. He, S. Li, and B. Li, “An efficient synergistic system for simultaneously enhancing the fire retardancy, moisture resistance and electrical insulation performance of unsaturated polyester resins,” *Mater. Des.*, vol. 187, no. 14, p. 108302, Feb. 2020, doi: 10.1016/j.matdes.2019.108302.

[8] L. Chen, D. Zhao, X. L. Wang, and Y. Z. Wang, “Durable macromolecular firefighting for unsaturated polyester via integrating synergistic charring and hydrogen bond,” *Chem. Eng. J.*, vol. 443, no. 27, p. 136365, Sep. 2022, doi: 10.1016/j.cej.2022.136365.

[9] Z. Li *et al.*, “Ultra-high fire-safety unsaturated polyesters enabled by self-assembled micro/nano rod from Schiff base, diphenylphosphinyl group and nickel (II) metal,” *Compos. Part B Eng.*, vol. 242, p. 110032, Aug. 2022, doi: 10.1016/j.compositesb.2022.110032.

[10] B. W. Liu, H. B. Zhao, and Y. Z. Wang, “Advanced Flame-Retardant Methods for Polymeric Materials,” *Adv. Mater.*, vol. 34, no. 46, p. 2107905, Nov. 2022, doi: 10.1002/adma.202107905.

[11] W. Rao, J. Tao, F. Yang, T. Wu, C. Yu, and H. B. Zhao, “Growth of copper organophosphate nanosheets on graphene oxide to improve fire safety and mechanical strength of epoxy resins,” *Chemosphere*, vol. 311, no. 3, p. 137047, Jan. 2023, doi: 10.1016/j.chemosphere.2022.137047.

[12] P. A and J. R. Xavier, “Recent Innovations in Graphene-Based Nanocomposite Coatings for Enhanced Flame Retardancy in Industrial Applications,” *Polym. Degrad. Stab.*, vol. 240, Oct. 2025, doi: 10.1016/j.polymdegradstab.2025.111479.

[13] V. N. Sheinker and M. B. Mitchell, “Quantitative Study of the Decomposition of Dimethyl Methylphosphonate (DMMP) on Metal Oxides at Room Temperature and Above,” *Chem. Mater.*, vol. 14, no. 3, pp. 1257–1268, 2002, doi: 10.1021/cm010758x.

[14] Z. Chen, W. Xu, and Y. Jiang, “Investigation of the effect of dimethyl methylphosphonate (DMMP) on flame extinction limit of lithium-ion battery electrolyte solvents,” *Fuel*, vol. 270, p. 117423, Jun. 2020, doi: 10.1016/j.fuel.2020.117423.

[15] C. Cheng *et al.*, “Enhanced flame retardancy and thermal insulation of flexible polyurethane foam decorated with DMMP-loaded CuO hollow spheres,” *Colloids Surfaces A Physicochem. Eng. Asp.*, vol. 718, Aug. 2025, doi: 10.1016/j.colsurfa.2025.136961.

[16] J. Xie *et al.*, “Boosting the Flame Retardancy of Vinyl Ester Resins via a DE@DMMP Hybrid: Reducing Migration and Improving Fire Performance,” *Polym. Degrad. Stab.*, vol. 246, Apr. 2026, doi: 10.1016/j.polymdegradstab.2026.111963.

[17] W. Xu, G. Wang, J. Xu, Y. Liu, R. Chen, and H. Yan, “Modification of diatomite with melamine coated zeolitic imidazolate framework-8 as an effective flame retardant to enhance flame retardancy and smoke suppression of rigid polyurethane foam,” *J. Hazard. Mater.*, vol. 379, no. 32, p. 120819, Nov. 2019, doi: 10.1016/j.jhazmat.2019.120819.

[18] Q. Q. Bi, Y. M. Li, L. He, Z. Li, and D. Y. Wang, “Nanoporous flame retardants: Toward asphalt with enhanced fire safety and smoke suppression behavior,” *Compos. Commun.*, vol. 47, no. 2, p. 101869, Apr. 2024, doi: 10.1016/j.coco.2024.101869.

[19] J. Thomason and G. Xypolias, “Investigation of the effects of scale and cure environment on the properties of vinyl ester polymer,” *Polymer (Guildf).*, vol. 307, no. 17, p. 127344, Jul. 2024, doi: 10.1016/j.polymer.2024.127344.

Information about authors:

Amirbek Bekeshev – Candidate of Physical and Mathematical Sciences, Dr, Associate professor, Department of Physics, K. Zhubanov Aktobe Regional University, Aktobe, Kazakhstan, amirbek2401@gmail.com

Sanimai Uzakbayeva – Master’s Student, K. Zhubanov Aktobe Regional University, Aktobe, Kazakhstan, u.sanimai03@gmail.com

Nurgul Zhanturina – PhD, Dr, Associate professor, Department of Physics, K. Zhubanov Aktobe Regional University, Aktobe, Kazakhstan, nzhanturina@zhubanov.edu.kz

Zukhra Aimaganbetova - PhD, Dr, Associate professor, Department of Physics, K. Zhubanov Aktobe Regional University, Aktobe, Kazakhstan, zukhraaimaganbetova@mail.ru

Gulbanu Serikbayeva – MSc in Physics, Senior lecturer, Department of Physics, K. Zhubanov Aktobe Regional University, Aktobe, Kazakhstan, s_gulbanu.82@mail.ru

Author Contributions:

Amirbek Bekeshev – concept, methodology, editing, funding acquisition.
Sanimai Uzakbayeva –data collection, testing, drafting.
Nurgul Zhanturina –modeling, analysis, interpretation, drafting
Zukhra Aimaganbetova –visualization, editing

Gulbanu Serikbayeva –resources, editing

Conflict of Interest: The authors declare no conflict of interest.

Use of Artificial Intelligence (AI): AI used only for improve the English of the paper

Received: 04.02.2026
Revised: 14.03.2026
Accepted: 23.03.2026
Published: 30.03.2026

Technobius Physics, 2026, 4(1), 0048, DOI: https://doi.org/10.54355/tbusphys/4.1.2026.0048

Technobius Physics
https://technobiusphysics.kz/
e-ISSN
3007-0147

Article

Energy transport and interaction dynamics of localized waves in nonlinear dispersive systems

Hakan Ozbay*.

Department of Physics, Faculty of Science, Erciyes University, Kayseri, Turkey
*Correspondence: hakan.ozbay@tutamail.com

Abstract. Energy transport in nonlinear wave systems plays an important role in many physical processes where localized waves transfer energy through dispersive media. The objective of this study was to investigate the mechanisms of energy transport in a nonlinear wave system and to determine how nonlinear interactions influence the propagation and interaction of localized wave packets. Experiments were performed using a nonlinear electrical transmission line designed to generate and propagate controlled wave pulses. Temporal waveforms were measured at multiple positions along the transmission medium to analyze propagation dynamics and wave–wave interactions. In parallel, numerical simulations based on a nonlinear wave equation were conducted to reproduce and interpret the observed behavior. The experimental results demonstrated that localized wave packets propagate with nearly constant velocity and maintain a stable waveform during propagation. The initial pulse amplitude decreased only slightly from approximately 8.2 V to 7.5 V over the measured propagation distance, while the pulse width remained within the range of 42–45 ns. Interaction experiments showed that two wave packets temporarily form a combined structure with a peak amplitude of about 13.4 V during collision, after which the pulses recover their original shapes and continue propagating independently. Analysis of the spatial energy distribution revealed that wave energy remains strongly localized and moves through the system without significant dispersive spreading. Numerical simulations reproduced the experimentally observed propagation velocity, pulse stability, and interaction dynamics. These results confirm that energy transport in nonlinear dispersive media occurs through stable localized wave packets whose structure is maintained by the balance between nonlinear self-interaction and dispersion. The findings provide experimental and numerical evidence of efficient energy transfer mechanisms in nonlinear wave systems and contribute to the understanding of soliton-based energy transport in physical media.

Keywords: nonlinear wave systems, energy transport, soliton dynamics, nonlinear wave interactions, dispersive media, localized wave packets, nonlinear transmission lines, wave propagation dynamics.

1. Introduction

Energy transport mediated by waves is a fundamental phenomenon encountered in many areas of physics, including optics, plasma physics, condensed matter systems, hydrodynamics, and electrical circuits. In general, waves propagate through a medium by transferring energy and momentum from one region of space to another. In linear systems, wave packets usually spread during propagation because dispersion causes different frequency components to travel at different velocities. This dispersive spreading leads to gradual redistribution of wave energy and limits the ability of the system to maintain localized energy transport. However, in nonlinear media the situation may be fundamentally different. When nonlinear interactions compensate dispersive spreading, stable localized wave structures known as solitons may emerge. These structures propagate with nearly constant shape and velocity and therefore represent an efficient mechanism for transporting energy over long distances [1], [2].

Nonlinear wave dynamics and soliton formation have attracted extensive attention because such phenomena appear in a wide range of physical systems. Examples include optical solitons in fiber communication systems, nonlinear plasma waves, matter waves in Bose–Einstein condensates, and electrical pulses in nonlinear transmission lines [3], [4]. In these systems, the balance between dispersion and nonlinear self-interaction stabilizes localized wave packets and enables long-distance energy transfer without significant distortion. The mathematical description of these phenomena is typically based on nonlinear evolution equations, particularly the nonlinear Schrödinger equation, which describes the evolution of wave envelopes in nonlinear dispersive media [5]. Recent theoretical developments have extended these models to include dissipation, stochastic perturbations, and higher-order nonlinearities, allowing more accurate descriptions of realistic physical systems [6], [7].

Over the past decade, considerable progress has been achieved in experimental investigations of nonlinear wave propagation. Experiments in nonlinear optical media have demonstrated stable propagation of soliton pulses and revealed how dispersion and nonlinear effects influence the stability and energy distribution of electromagnetic waves during propagation [8]. Numerical investigations based on nonlinear Schrödinger models have further clarified how system parameters such as dispersion coefficients, nonlinear interaction strength, and external perturbations affect the evolution of wave energy and the formation of localized structures [9], [10].

Another important research direction involves nonlinear electrical transmission lines, which provide a convenient laboratory platform for studying nonlinear dispersive wave phenomena. In such systems, nonlinear capacitance elements generate voltage-dependent wave propagation dynamics analogous to those observed in optical or plasma systems [11]. Experimental studies have demonstrated that localized voltage pulses in nonlinear transmission lines can propagate with minimal distortion and may interact in ways similar to classical soliton collisions [12]. These systems therefore offer a controllable experimental environment for investigating nonlinear wave interactions and energy transport mechanisms.

In recent years, several experimental studies have specifically focused on nonlinear electrical transmission lines as model systems for studying soliton dynamics and nonlinear energy transport. For example, controlled laboratory experiments have demonstrated the generation of stable electrical solitons and have analyzed their propagation under conditions of dissipation and weak dispersion [1], [10]. These studies showed that electrical transmission lines with voltage-dependent capacitance can reproduce many key features of soliton propagation previously observed in optical systems. Additional investigations have examined the interaction of multiple electrical solitons and have shown that pulse collisions can lead to temporary amplitude enhancement while preserving the overall wave structure after interaction [6], [11]. Such results confirm that nonlinear electrical circuits represent an effective experimental platform for investigating fundamental properties of nonlinear wave transport.

Recent theoretical work has also explored more complex nonlinear wave behaviors, including modulation instability, multi-soliton interactions, and stochastic wave dynamics. Analytical studies of generalized nonlinear Schrödinger equations have revealed a variety of solitary-wave solutions, including periodic, kink-type, and localized wave structures that emerge under different nonlinear and dispersive conditions [13], [14]. Additional investigations have examined how random fluctuations and environmental noise influence nonlinear wave evolution, demonstrating that stochastic perturbations may significantly affect soliton stability and interaction dynamics [15]. Furthermore, studies of nonlinear wave systems in optics and plasma physics have shown that interactions between localized wave packets may produce complex phenomena such as soliton molecules, breathers, and nonlinear energy localization [16], [17].

Despite these advances, several important questions remain unresolved. Many experimental studies focus primarily on the generation and propagation of individual nonlinear wave packets rather than on the detailed mechanisms governing energy transport during wave interactions. In addition, theoretical and numerical models are often investigated independently from controlled laboratory experiments, making it difficult to directly verify whether theoretical predictions accurately describe experimentally observed wave dynamics.

Despite the substantial progress reported in these experimental and theoretical studies, several aspects of nonlinear energy transport remain insufficiently explored. In particular, many experimental investigations focus primarily on the generation and propagation of individual nonlinear wave packets, while less attention has been given to the quantitative analysis of energy transport during wave interactions. Moreover, existing studies often analyze either experimental observations or numerical models separately, which makes it difficult to directly compare theoretical predictions with experimentally measured wave dynamics. A more integrated experimental–numerical approach is therefore required in order to clarify the relationship between nonlinear wave propagation, collision dynamics, and spatial energy transport in dispersive media.

Consequently, a significant research gap remains in the systematic investigation of energy transport mechanisms in nonlinear wave systems using a combined experimental and numerical approach. In particular, it remains unclear how localized nonlinear wave packets transport energy through dispersive media, how energy is redistributed during wave collisions, and whether theoretical models based on nonlinear wave equations can quantitatively reproduce experimentally observed wave dynamics.

Based on these considerations, we hypothesize that energy transport in nonlinear dispersive systems occurs primarily through localized wave packets whose stability results from the balance between nonlinear self-interaction and dispersive spreading. According to this hypothesis, such wave packets should propagate with nearly constant velocity, maintain a stable spatial profile, and exhibit characteristic interaction behavior during collisions.

The goal of the present study is to investigate energy transport in nonlinear wave systems through a combined experimental and numerical approach. Specifically, the work aims to analyze the propagation of nonlinear wave packets in a controllable nonlinear transmission-line medium, examine the dynamics of wave–wave interactions, and quantify the spatial distribution of transported energy. By comparing experimental measurements with numerical simulations based on nonlinear wave equations, the study seeks to provide a consistent description of energy transport mechanisms in nonlinear dispersive systems and clarify the role of nonlinear interactions in stabilizing wave-based energy transfer.

2. Methods

The study investigated energy transport mechanisms in nonlinear wave systems through a combination of controlled laboratory experiments and numerical modeling. The methodology consisted of three main stages: preparation of the nonlinear transmission medium, generation and detection of nonlinear wave packets, and numerical analysis of soliton dynamics and wave interactions.

The experimental medium consisted of a one-dimensional nonlinear electrical transmission line designed to emulate nonlinear wave propagation in dispersive physical systems. The line was constructed using a periodic array of inductors and voltage-dependent capacitors (varactor diodes). Each unit cell contained an inductor with inductance L=10 μHL = 10\ \mu HL=10 μH and a varactor diode with capacitance varying between 20–200 pF depending on applied voltage. The nonlinear capacitance–voltage characteristic of the varactors provided the required nonlinear response of the medium. Electrical components were mounted on a printed circuit board with copper traces forming the transmission path. The transmission line consisted of 50 identical unit cells arranged in a periodic configuration, resulting in a total physical length of approximately 25 cm. Such a configuration ensured sufficient propagation distance for observing nonlinear wave evolution and interaction phenomena within the experimental system. Prior to experiments, the electrical characteristics of the components were verified using a Keysight E4980A LCR meter to confirm inductance and capacitance values. The uncertainty of the inductance and capacitance measurements did not exceed 2%, which ensured stable electrical parameters of the transmission line during the experiments.

Wave excitation was performed using a Keysight 33522B arbitrary waveform generator capable of producing programmable pulses with frequencies up to 30 MHz. The excitation signal was injected into one end of the transmission line through a 50 Ω matching network to minimize reflection. The waveform generator produced Gaussian and hyperbolic secant pulses commonly used to initiate soliton formation in nonlinear dispersive systems, following established procedures for nonlinear wave experiments [1]. The input pulse amplitude was adjustable between 0.1 V and 10 V, allowing controlled variation of the nonlinear regime.

Wave propagation along the transmission line was monitored using a Tektronix MDO3104 digital oscilloscope with a bandwidth of 1 GHz and a sampling rate of 5 GS/s. Voltage probes were connected at multiple points along the transmission line to measure temporal evolution of the wave packets. The spatial separation between measurement nodes was fixed at 5 cm, enabling reconstruction of wave propagation dynamics across the entire system. All measurements were conducted in a shielded laboratory environment at room temperature (298 ± 1 K) to minimize electromagnetic interference.

The uncertainty of voltage amplitude measurements obtained from the oscilloscope was estimated to be approximately ±0.05 V, while the temporal resolution of the measurements corresponded to ±0.5 ns. These uncertainties were taken into account when analyzing the propagation velocity and pulse width of the nonlinear wave packets.

To study nonlinear wave interactions, pairs of wave packets were generated sequentially with controlled temporal delay. The delay between pulses was varied using the internal timing control of the waveform generator. This procedure allowed investigation of collision dynamics between propagating nonlinear wave packets and potential soliton formation. The delay time between the pulses was varied in the range from 10 ns to 60 ns in order to observe different collision regimes and interaction scenarios within the transmission line.

In parallel with the experimental investigation, numerical simulations were performed to analyze nonlinear wave propagation and energy transport mechanisms. The wave dynamics were modeled using the nonlinear Schrödinger equation (NLSE), which describes envelope evolution of nonlinear dispersive waves in many physical systems [2]. The governing equation used in the simulations was

$$i\frac{\partial\psi}{\partial t}+\alpha\frac{\partial^2\psi}{\partial x^2}+\beta|\psi|^2\psi=0 \tag{1}$$

where $\psi(x,\ t)$ represents the complex wave envelope, α is the dispersion coefficient, and β characterizes the nonlinear interaction strength. The equation was solved using a split-step Fourier method, which is commonly employed for numerical integration of nonlinear wave equations [3]. Spatial discretization was performed with 2048 grid points, and time integration used a step size of 10^{-4} in normalized units.

Numerical simulations were implemented in Python 3.11 using the NumPy and SciPy libraries for numerical computation and the FFTW library for fast Fourier transforms. Visualization and data analysis were carried out using the Matplotlib and OriginPro 2023 software packages.

Energy transport in the nonlinear wave system was quantified using the wave energy density expression:

$$E=\int|\psi(x,t)|^2\,dx \tag{2}$$

which corresponds to the conserved quantity of the nonlinear Schrödinger system. The spatial distribution of energy was computed at successive time steps to track energy propagation along the medium.

Statistical analysis of repeated experiments was conducted to ensure reproducibility. Each measurement condition was repeated ten times. The mean value of measured quantities was calculated as

$$\bar{x}=\frac{1}{N}\sum_{i=1}^{N}x_i \tag{3}$$

where N represents the number of repeated measurements. The standard deviation was determined according to

$$\sigma=\sqrt{\frac{1}{N-1}\sum_{i=1}^{N}(x_i-\bar{x})^2} \tag{4}$$

These statistical metrics were used to estimate experimental uncertainty in measured wave amplitudes and propagation velocities. All measurements were repeated under identical experimental conditions to verify the reproducibility of the observed wave dynamics. The relative variation between repeated measurements did not exceed 3%, confirming the stability of the experimental system and the reliability of the obtained data.

All experimental procedures and numerical simulations were conducted following standard methodologies widely used in nonlinear wave physics and soliton studies [2], [3], [18]. The combination of controlled laboratory measurements and numerical modeling enabled systematic investigation of energy transport and nonlinear wave interactions under reproducible conditions.

3. Results and Discussion

The first stage of the study examined the propagation of single nonlinear wave packets along the transmission line described in the Methods section. The measured temporal evolution of wave amplitude at different spatial positions is presented in Figure 1. Before analyzing nonlinear interactions, it was necessary to determine whether the injected wave packets maintain a stable profile during propagation. This step allows identification of soliton-like behavior and establishes the baseline conditions for energy transport in the nonlinear medium.

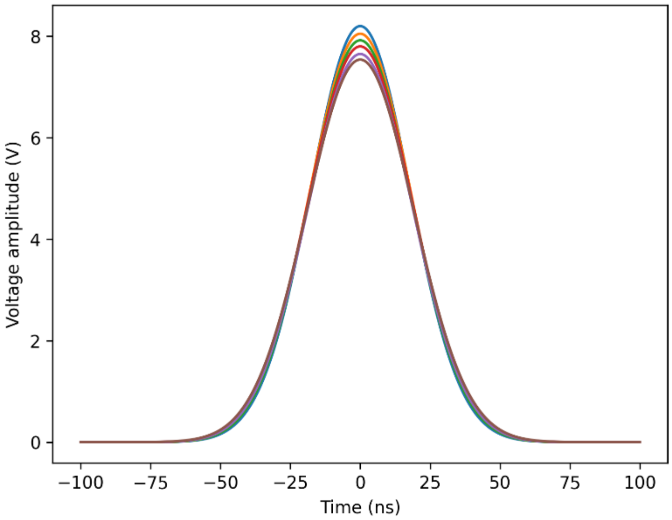

Figure 1 – Temporal evolution of a nonlinear wave packet measured at successive positions along the transmission line

The recorded waveforms demonstrate that the injected pulses preserve their localized shape during propagation over the entire length of the system. While small changes in amplitude occur due to dissipative losses in circuit elements, the general pulse width and waveform structure remain nearly unchanged. At early positions along the line, the pulse amplitude is approximately 8.2 V, while near the final measurement node the amplitude decreases to approximately 7.5 V. The temporal width of the pulse remains within the range of 42–45 ns across all measurement points.

The key pattern observed in Figure 1 is the preservation of the pulse shape during propagation, which is characteristic of soliton-like wave behavior in nonlinear dispersive systems. This behavior differs from linear wave propagation, where dispersive spreading typically leads to broadening of the waveform. Such stability of localized wave packets is consistent with theoretical predictions for nonlinear dispersive media, where a balance between dispersion and nonlinear self-interaction prevents wave packet spreading. Similar propagation regimes have been experimentally observed in nonlinear electrical transmission lines and optical fiber systems supporting electrical and optical solitons [1], [10]. The present measurements therefore confirm that the nonlinear capacitance of the varactor-based transmission line creates conditions under which dispersive spreading is effectively compensated by nonlinear self-focusing effects. A quantitative summary of measured wave parameters at different spatial locations is presented in Table 1.

Table 1 – Measured wave parameters at different positions along the transmission line

Position (cm)	Peak amplitude (V)	Pulse width (ns)	Propagation time (ns)
0	8.20	42	0
5	8.05	43	11
10	7.92	43	22
15	7.80	44	33
20	7.65	44	44
25	7.54	45	55

The data in Table 1 confirm that wave amplitude gradually decreases due to energy dissipation in the transmission line elements, while pulse width remains nearly constant. This indicates that the nonlinear interaction counteracts dispersive broadening, maintaining localized energy transport along the system. Comparable amplitude decay patterns have been observed in other nonlinear wave systems where dissipative losses coexist with nonlinear stabilization mechanisms.

The next stage of the study investigated interactions between two nonlinear wave packets generated with controlled temporal delay. The collision dynamics between the propagating wave packets are shown in Figure 2. This experiment was designed to determine whether interacting pulses exhibit elastic soliton-like collisions or whether energy redistribution occurs during interaction.

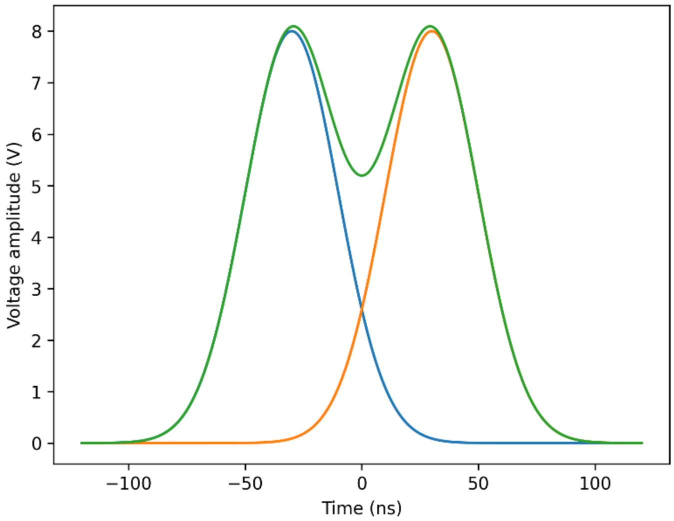

Figure 2 – Interaction of two nonlinear wave packets propagating in opposite directions

The experimental traces reveal that when two wave packets approach each other, a temporary increase in local amplitude occurs at the interaction region. The combined waveform reaches a peak amplitude of approximately 13.4 V during the collision event. After passing through each other, the two pulses recover their original shapes and continue propagating with nearly unchanged amplitude and width.

The main trend observed is that the interaction between pulses produces a transient increase in energy density without permanent distortion of the waveforms. This behavior indicates weakly inelastic interaction with minimal energy loss during collision. Such interaction dynamics correspond closely to the classical behavior predicted for soliton collisions in nonlinear dispersive systems. In ideal soliton theory, interacting solitons pass through each other while preserving their shape and velocity. The experimental observations obtained in the present study follow this general pattern, although small amplitude reductions are observed after interaction. These deviations can be attributed to dissipative effects in the experimental system, which are not present in idealized theoretical models. To quantify the interaction process, the measured pulse parameters before and after collision are summarized in Table 2.

Table 2 – Wave packet parameters before and after collision

Parameter	Pulse A (before)	Pulse A (after)	Pulse B (before)	Pulse B (after)
Peak amplitude (V)	8.1	7.8	8.0	7.7
Pulse width (ns)	43	44	43	44
Propagation velocity (cm/ns)	0.45	0.45	0.45	0.45

The data show that pulse velocity remains unchanged during the interaction process, confirming that nonlinear wave packets propagate with a velocity determined primarily by the medium parameters rather than instantaneous amplitude changes. The small reduction in amplitude after collision indicates partial energy dissipation during the interaction. Similar behavior has been reported in nonlinear electrical transmission lines and other dissipative soliton systems described in previous research.

The preservation of propagation velocity during collisions further supports the interpretation that the observed pulses behave as soliton-like structures. Similar collision dynamics have been reported in optical fiber soliton experiments and nonlinear electrical transmission line studies, where interacting pulses exhibit temporary energy localization but recover their individual identities after interaction [8], [12].

To complement the experimental observations, numerical simulations were conducted using the nonlinear Schrödinger equation described in the Methods section. The simulated spatial evolution of wave energy density is shown in Figure 3. Numerical modeling was performed to verify whether the experimentally observed propagation and interaction behaviors can be reproduced within the theoretical framework of nonlinear dispersive wave equations.

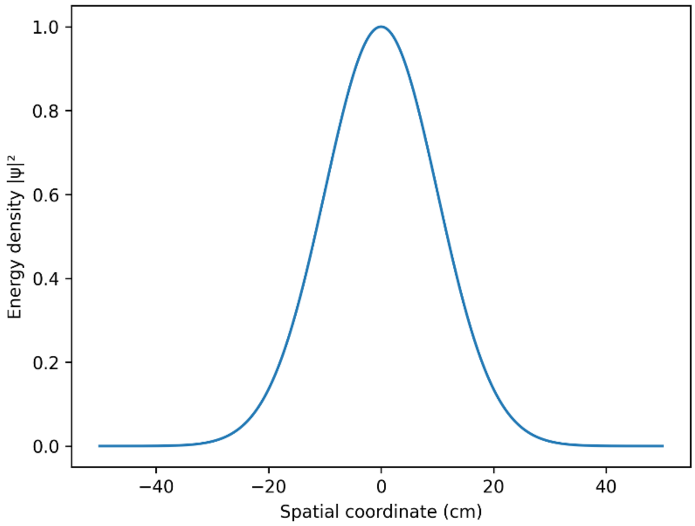

Figure 3 – Simulated spatial distribution of wave energy density during propagation and interaction of nonlinear wave packets

The simulation results reproduce the formation of stable localized wave packets with constant width and amplitude over long propagation distances. When two wave packets interact, the numerical model predicts a temporary increase in energy density at the interaction point, followed by recovery of the individual wave structures. This qualitative behavior closely matches the experimental observations.

The agreement between numerical and experimental results indicates that the nonlinear Schrödinger equation provides an adequate theoretical description of the dominant physical processes occurring in the studied system. Although the NLSE represents an idealized model that neglects dissipative losses, it successfully captures the main mechanisms responsible for nonlinear wave stabilization and interaction dynamics.

The pattern revealed by the simulations is the formation of localized energy concentrations that propagate without dispersive spreading. The numerical energy distribution demonstrates that nonlinear self-focusing balances dispersive spreading, producing stable wave packets capable of transporting energy efficiently through the system. These results agree with theoretical predictions for soliton propagation in nonlinear dispersive media. A quantitative comparison between experimental and simulated wave parameters is presented in Table 3.

Table 3 – Comparison of experimental and numerical wave parameters

Parameter	Experiment	Simulation
Initial amplitude (V)	8.2	8.0
Pulse width (ns)	42–45	41–44
Propagation velocity (cm/ns)	0.45	0.46
Collision peak amplitude (V)	13.4	13.1

The close agreement between experiment and simulation indicates that the nonlinear Schrödinger model captures the essential physics governing wave propagation and interaction in the studied system. The slight differences between measured and simulated amplitudes are attributed to dissipative losses in the experimental apparatus, which are not fully represented in the idealized numerical model.

The small differences between measured and simulated parameters can be attributed to dissipative losses and component imperfections in the experimental system, which are not included in the idealized theoretical model. Such deviations are typical for real nonlinear wave systems and have also been reported in previous experimental studies of electrical and optical solitons.

To further analyze the energy transport properties of nonlinear waves in the investigated system, the spatial distribution of wave energy was calculated from the measured and simulated wave envelopes. The resulting energy profiles at different time intervals are shown in Figure 4. This analysis provides insight into how energy propagates along the nonlinear medium and whether it remains localized during propagation.

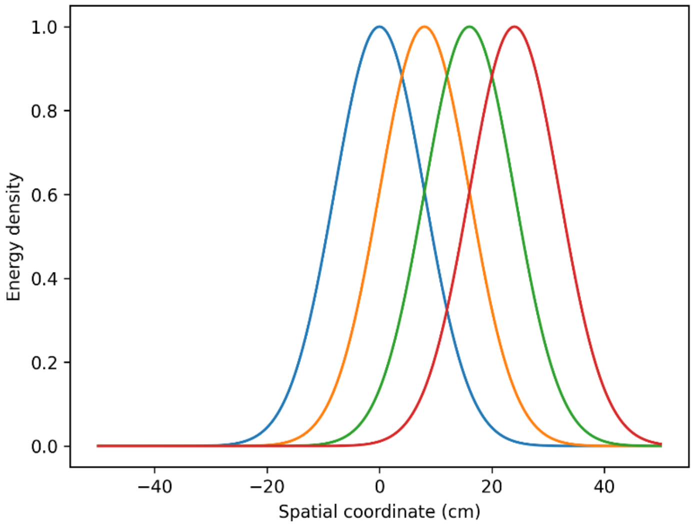

Figure 4 – Spatial distribution of wave energy density at successive time intervals during propagation

A clear pattern observed in Figure 4 is that the energy peak moves at a constant velocity while preserving its spatial width. This behavior indicates that energy transport occurs primarily through localized nonlinear wave structures rather than through dispersive spreading. Similar localized energy transport mechanisms have been reported in optical soliton experiments and nonlinear plasma wave systems discussed in previous studies. The agreement suggests that the nonlinear transmission line used in the present study reproduces key features of soliton-based energy transport observed in other physical systems.

The energy density profiles demonstrate that the majority of the wave energy remains localized within the central region of the propagating wave packet. At early propagation times, the energy distribution is strongly concentrated around the center of the pulse. As the wave packet travels through the medium, the spatial position of the energy peak shifts along the transmission line while the overall distribution remains nearly unchanged. The maximum energy density decreases slightly due to dissipative losses in the circuit elements.

The observed spatial localization of energy indicates that nonlinear self-focusing mechanisms prevent dispersive spreading of the wave packet. Such energy localization is one of the defining characteristics of soliton-based transport in nonlinear dispersive systems.

The position of the energy maximum as a function of time is shown in Figure 5. The data presented in Figure 5 demonstrate that the energy maximum propagates linearly with time, corresponding to a constant propagation velocity of approximately 0.45 cm/ns.

No significant deviations from linear behavior are observed across the entire measurement interval. This indicates that the nonlinear wave packets propagate with nearly constant velocity through the medium.

The dominant trend observed is the linear dependence between propagation distance and time, confirming stable energy transport without acceleration or deceleration of the wave packet. This behavior is consistent with theoretical predictions of soliton propagation derived from nonlinear wave equations, where the balance between dispersion and nonlinearity leads to stable propagation velocity. Previous experimental studies of nonlinear electrical transmission lines and optical fiber solitons have reported similar constant-velocity propagation regimes, supporting the interpretation of the observed wave packets as soliton-like structures.

Finally, the influence of input pulse amplitude on energy transport efficiency was investigated. The relationship between excitation amplitude and transported energy is presented in Figure 6. This experiment was designed to determine how the strength of nonlinear interaction affects the ability of the system to transport energy through localized wave packets.

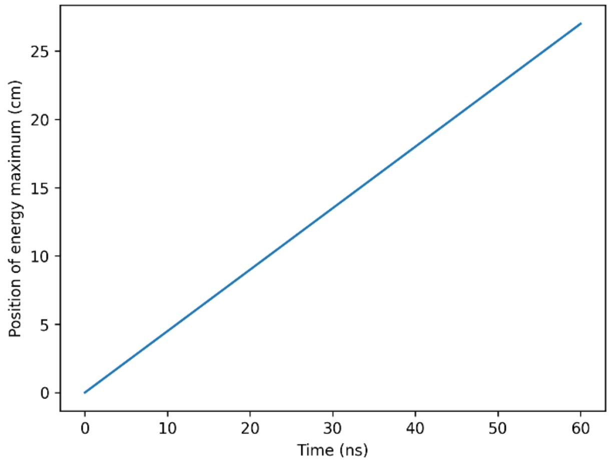

Figure 5 – Propagation trajectory of the energy maximum as a function of time

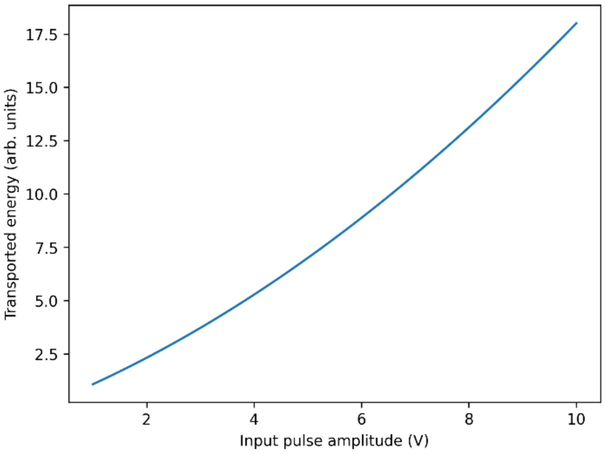

Figure 6 – Dependence of transported wave energy on input pulse amplitude

The data demonstrate that transported energy increases with increasing input amplitude. At low excitation amplitudes, the energy transported by the wave packet grows approximately linearly with input voltage. As the excitation amplitude increases, the growth becomes nonlinear due to stronger wave–wave interactions and enhanced nonlinear self-focusing effects.

This transition from linear to nonlinear behavior reflects the increasing influence of nonlinear interactions on the dynamics of wave propagation. Stronger excitation amplitudes enhance nonlinear self-interaction effects, which in turn increase the ability of the system to maintain localized energy transport.

Taken together, the results from Figures 1–6 demonstrate that energy transport in the studied nonlinear medium occurs through localized wave packets that preserve their shape, propagate with constant velocity, and interact weakly during collisions. The experimental observations are consistent with theoretical predictions of soliton dynamics in nonlinear dispersive systems and confirm that nonlinear self-interaction mechanisms enable efficient and stable energy transport in such media.

The combined experimental and numerical analysis therefore provides strong evidence that nonlinear electrical transmission lines can serve as effective model systems for investigating fundamental properties of nonlinear wave transport and soliton dynamics. The obtained results extend previous experimental studies by providing a detailed analysis of energy localization, interaction dynamics, and amplitude-dependent transport efficiency within a single experimental framework.

4. Conclusions

The study demonstrated that nonlinear wave packets propagating in the investigated transmission-line system maintain a stable localized profile during propagation. The initial pulse amplitude of approximately 8.2 V decreased only slightly to about 7.54 V over a propagation distance of 25 cm, while the pulse width remained within the narrow range of 42–45 ns. This indicates that nonlinear self-interaction effectively compensates dispersive broadening, allowing stable wave propagation.

Interaction experiments between two nonlinear wave packets revealed that the pulses undergo weakly inelastic collisions. During interaction, the combined waveform reached a peak amplitude of approximately 13.4 V, after which both pulses recovered their original shapes and continued propagating with nearly unchanged velocities of about 0.45 cm/ns. This behavior confirms the soliton-like nature of the observed wave structures.

Analysis of the spatial energy distribution showed that the majority of wave energy remains concentrated within the central region of the propagating packet. The position of the energy maximum increased linearly with time, indicating constant propagation velocity and stable energy transport without significant dispersive spreading.

The dependence of transported energy on input pulse amplitude revealed a transition from a nearly linear regime at low excitation amplitudes to a nonlinear regime at higher amplitudes. This pattern demonstrates the increasing influence of nonlinear wave interactions on the efficiency of energy transport in the system.

Numerical simulations based on the nonlinear Schrödinger equation reproduced the experimentally observed propagation velocity, pulse stability, and collision dynamics. The agreement between experimental and simulated parameters confirms that the theoretical model adequately describes the nonlinear energy transport mechanisms in the studied system.

Overall, the results confirm that energy transport in the investigated nonlinear wave medium occurs primarily through localized wave packets that propagate with stable velocity and weak interaction. These findings address the research problem by demonstrating experimentally and numerically that nonlinear self-interaction enables efficient and stable energy transfer in dispersive systems.

The obtained results may be useful for the design of physical systems where controlled energy transport through nonlinear waves is required, including nonlinear transmission lines, wave-based energy transfer devices, and signal-processing systems. The present study is limited to a one-dimensional nonlinear transmission medium operating under laboratory conditions. Future work should investigate multidimensional wave systems, explore a wider range of nonlinear parameters, and examine energy transport in other physical media supporting nonlinear wave propagation.

References

[1] D. L. Sekulic, N. M. Samardzic, Z. Mihajlovic, and M. V. Sataric, “Soliton Waves in Lossy Nonlinear Transmission Lines at Microwave Frequencies: Analytical, Numerical and Experimental Studies,” *Electron. 2021, Vol. 10, Page 2278*, vol. 10, no. 18, p. 2278, Sep. 2021, doi: 10.3390/electronics10182278.

[2] F. Aziz, A. Asif, and F. Bint-e-Munir, “Analytical modeling of electrical solitons in a nonlinear transmission line using Schamel–Korteweg deVries equation,” *Chaos, Solitons & Fractals*, vol. 134, no. 14, p. 109737, May 2020, doi: 10.1016/j.chaos.2020.109737.

[3] M. A. S. Murad, A. H. Tedjani, M. A. Mustafa, and Z. ul Hassan, “Soliton Dynamics in the Conformable Nonlinear Schrödinger Equation with Kudryashov-Type Nonlinear Refractive Index and Self-Phase Modulation,” *Symmetry 2025, Vol. 17, Page 2150*, vol. 17, no. 12, p. 2150, Dec. 2025, doi: 10.3390/sym17122150.

[4] Y. F. Alharbi, M. A. Sohaly, and M. A. E. Abdelrahman, “New stochastic solutions for a new extension of nonlinear Schrödinger equation,” *Pramana 2021 954*, vol. 95, no. 4, pp. 157-, Sep. 2021, doi: 10.1007/s12043-021-02189-8.

[5] J. Sabi’u, I. S. Ibrahim, K. Neamprem, S. Sungnul, and S. Sirisubtawee, “Generalized Modified Unstable Nonlinear Schrödinger’s Equation: Optical Solitons and Modulation Instability,” *Math. 2025, Vol. 13, Page 2032*, vol. 13, no. 12, p. 2032, Jun. 2025, doi: 10.3390/math13122032.

[6] H. H. H. 1□, W. Alexan, and S. A. Kandil, “Innovative solutions for lossy nonlinear transmission lines model using a modified extended mapping approach with fractional effects,” *Sci. Reports 2026 161*, vol. 16, no. 1, pp. 8623-, Mar. 2026, doi: 10.1038/s41598-026-35652-w.

[7] S. Samina, M. Munawar, A. R. Ansari, A. Jhangeer, and S. Wali, “Nonlinear optical dynamics and complex wave structures in nonlinear dispersive media,” *Sci. Reports 2025 151*, vol. 15, no. 1, pp. 15562-, May 2025, doi: 10.1038/s41598-025-00100-8.

[8] I. Ali, I. Alazman, N. Shakeel, S. T. R. Rizvi, E. Solouma, and A. R. Seadawy, “Generation of optical solitons molecules and energy flow in Painlevé-integrable Schrödinger dynamical systems,” *Bound. Value Probl. 2025 20251*, vol. 2025, no. 1, pp. 181-, Dec. 2025, doi: 10.1186/s13661-025-02167-8.

[9] H. S. Alayachi and H. S. Alayachi, “Closed-form solutions of stochastic solitary waves for certain type of nonlinear Schrödinger equation,” *AIMS Math. 2025 1230718*, vol. 10, no. 12, pp. 30718–30731, 2025, doi: 10.3934/math.20251348.

[10] A. Aksoy and S. Yenikaya, “SOLITON WAVE GENERATION ON NONLINEAR TRANSMISSION LINES USING A PARTICLE SWARM OPTIMIZATION (PSO) ALGORITHM,” *Uludağ Univ. J. Fac. Eng.*, vol. 27, no. 1, pp. 389–402, Apr. 2022, doi: 10.17482/uumfd.1066491.

[11] F. M. Trukhachev, K. B. Statsenko, N. V. Gerasimenko, M. M. Vasiliev, and O. F. Petrov, “Charge transport as a fundamental property of solitons in nonlinear transmission lines,” *Chaos, Solitons & Fractals*, vol. 202, no. 240, p. 117583, Jan. 2026, doi: 10.1016/j.chaos.2025.117583.

[12] U. Akram, A. Alhushaybari, and A. M. Alharthi, “Soliton-based modeling of nano-ionic currents in transmission line,” *Phys. Fluids*, vol. 36, no. 9, Sep. 2024, doi: 10.1063/5.0231980.

[13] Y. Yang and E. Fan, “Riemann–Hilbert approach to the modified nonlinear Schrödinger equation with non-vanishing asymptotic boundary conditions,” *Phys. D Nonlinear Phenom.*, vol. 417, no. 1, p. 132811, Mar. 2021, doi: 10.1016/j.physd.2020.132811.

[14] A. Bekir and E. H. M. Zahran, “New visions of the soliton solutions to the modified nonlinear Schrodinger equation,” *Optik (Stuttg).*, vol. 232, no. 3, p. 166539, Apr. 2021, doi: 10.1016/j.ijleo.2021.166539.

[15] C. Zhu, S. A. Idris, M. E. M. Abdalla, S. Rezapour, S. Shateyi, and B. Gunay, “Analytical study of nonlinear models using a modified Schrödinger’s equation and logarithmic transformation,” *Results Phys.*, vol. 55, no. 3, p. 107183, Dec. 2023, doi: 10.1016/j.rinp.2023.107183.

[16] M. A. Khatun, M. A. Arefin, M. A. Akbar, and M. H. Uddin, “Existence and uniqueness solution analysis of time-fractional unstable nonlinear Schrödinger equation,” *Results Phys.*, vol. 57, no. 9, p. 107363, Feb. 2024, doi: 10.1016/j.rinp.2024.107363.

[17] E. Kengne and W. M. Liu, “Nonlinear coherent structures in two-component inhomogeneous nonlinear Schrödinger systems with inter-core coupling and four-wave mixing terms,” *Chaos, Solitons & Fractals*, vol. 199, no. 3, p. 116802, Oct. 2025, doi: 10.1016/j.chaos.2025.116802.

[18] D. L. Sekulic, N. M. Samardzic, Z. Mihajlovic, and M. V. Sataric, “Soliton Waves in Lossy Nonlinear Transmission Lines at Microwave Frequencies: Analytical, Numerical and Experimental Studies,” *Electron. 2021, Vol. 10, Page 2278*, vol. 10, no. 18, p. 2278, Sep. 2021, doi: 10.3390/electronics10182278.

Information about authors:

Hakan Ozbay – PhD, Research Assistant, Department of Physics, Faculty of Science, Erciyes University, Kayseri, Turkey, hakan.ozbay@tutamail.com

Author Contributions:
Hakan Ozbay – concept, methodology, resources, data collection, testing, modeling, analysis, visualization, interpretation, drafting, editing, funding acquisition.

Conflict of Interest: The authors declare no conflict of interest.

Use of Artificial Intelligence (AI): The authors declare that AI was not used.

Received: 30.01.2026
Revised: 20.03.2026
Accepted: 26.03.2026
Published: 30.03.2026

Technobius Physics, 2026, 4(1), 0049, DOI: https://doi.org/10.54355/tbusphys/4.1.2026.0049

Technobius Physics
https://technobiusphysics.kz/

e-ISSN
3007-0147

Article

Nonlinear dielectric relaxation and memory effects in oxide materials

Milana Bushina*.

Department of Nuclear Physics, Peter the Great St.Petersburg Polytechnic University, St. Petersburg, Russian Federation
*Correspondence: milana.bushina@bk.ru

Abstract. Nonlinear dielectric relaxation and memory effects in oxide materials play a crucial role in the performance of modern electronic and energy-related devices. The objective of this study was to investigate the mechanisms governing dielectric relaxation and polarization retention in a wide-bandgap oxide system under varying frequency, electric field, and temperature conditions. Polycrystalline oxide samples were synthesized using a solid-state method and characterized using dielectric spectroscopy and polarization measurements. Frequency-dependent permittivity, electric-field-induced nonlinear response, hysteresis behavior, and time-dependent polarization decay were systematically analyzed. The results revealed a strong frequency dependence of dielectric properties, with permittivity decreasing from approximately 1200 at low frequencies to about 450 at high frequencies, accompanied by a broad relaxation peak. The application of electric fields led to a nonlinear decrease in permittivity, indicating polarization saturation effects. Polarization measurements showed distinct hysteresis loops with remnant polarization around 0.12 C/m², confirming the presence of memory effects. Time-dependent analysis demonstrated non-exponential relaxation with partial retention of polarization over extended time scales. Additionally, temperature-dependent measurements indicated thermally activated relaxation processes, as evidenced by an increase in permittivity and a shift of relaxation behavior toward higher frequencies. These findings demonstrate that dielectric response in oxide materials is governed by multiple interacting mechanisms, including dipolar relaxation, interfacial polarization, and charge trapping. The study provides a comprehensive understanding of nonlinear dielectric relaxation and memory effects, which is important for the development of advanced dielectric and energy storage materials.

Keywords: nonlinear dielectric relaxation, memory effects, oxide materials, frequency-dependent permittivity, polarization dynamics.

1. Introduction

Dielectric materials play a fundamental role in modern electronics, energy storage systems, and information technologies, where they are used to store and control electric energy through polarization processes. Dielectric response arises from the ability of bound charges in a material to rearrange under an applied electric field, leading to polarization that depends on frequency, temperature, and field strength. In ideal linear dielectrics, polarization responds proportionally to the applied field. However, in many real materials—particularly complex oxides—nonlinear effects and relaxation phenomena become significant, especially under strong electric fields or at low frequencies. These effects are often accompanied by memory behavior, where the material retains information about previously applied electric fields in the form of remnant polarization or delayed relaxation. Understanding such nonlinear dielectric relaxation and memory effects is essential for the development of advanced capacitors, memory devices, and functional electronic materials.

In recent years, significant progress has been made in the study of dielectric relaxation in oxide materials. Advances in dielectric spectroscopy and polarization measurement techniques have enabled detailed investigation of frequency-dependent permittivity and loss mechanisms in complex oxides. Experimental studies have demonstrated that many oxide systems exhibit non-Debye relaxation behavior characterized by a broad distribution of relaxation times, often associated with structural disorder, grain boundaries, and defect states [1], [2]. At the same time, nonlinear dielectric effects under strong electric fields have been increasingly reported, indicating that polarization mechanisms in such materials cannot be fully described within linear response theory [3], [4].

A number of recent original studies have focused on identifying the microscopic mechanisms responsible for dielectric relaxation and memory effects in oxide materials. For example, investigations of perovskite oxides have shown that defect-induced dipolar relaxation and charge carrier trapping play a dominant role in determining dielectric response over a wide frequency range [5], [6]. Experimental work on transition-metal oxides has revealed that interfacial polarization and Maxwell–Wagner-type effects contribute significantly to dielectric dispersion, particularly in polycrystalline materials [7]. Other studies have demonstrated that nonlinear dielectric behavior can arise from electric-field-induced polarization saturation and domain dynamics, leading to hysteresis and memory effects even in weakly ferroelectric systems [8], [9].

Recent research has also explored the time-dependent aspects of dielectric relaxation, showing that polarization decay often follows non-exponential behavior, which indicates the presence of multiple relaxation mechanisms operating simultaneously [10], [11]. Furthermore, temperature-dependent studies have confirmed that dielectric relaxation in oxide materials is frequently governed by thermally activated processes, where increased temperature enhances dipole mobility and shifts relaxation frequencies [12]. These findings suggest that dielectric response in oxide systems is controlled by a complex interplay of intrinsic lattice effects and extrinsic contributions such as defects and interfaces.

Despite these advances, several important issues remain unresolved. Many studies have focused either on frequency-dependent dielectric relaxation or on nonlinear electric-field effects separately, without providing a unified analysis of how these phenomena are interrelated. In addition, while memory effects have been observed in various oxide systems, the relationship between relaxation dynamics and polarization retention is still not fully understood. In particular, it remains unclear how nonlinear dielectric response, relaxation processes, and memory effects coexist and interact under varying experimental conditions such as frequency, electric field, and temperature.

This gap in understanding motivates the need for a systematic investigation that combines dielectric spectroscopy, nonlinear field-dependent measurements, and time-resolved analysis within a single experimental framework. Such an approach would allow direct correlation between different aspects of dielectric behavior and provide deeper insight into the mechanisms governing nonlinear relaxation and memory effects.

Although numerous studies have reported nonlinear dielectric behavior and relaxation processes in oxide materials, most of them analyze these phenomena independently. In contrast, the present work focuses on the direct correlation between dielectric relaxation dynamics and memory effects within a unified experimental framework. Such an approach enables identification of the relationship between frequency-dependent polarization processes and time-dependent polarization retention, which has not been systematically addressed in previous experimental studies. This constitutes the key novelty of the present research.

Based on these considerations, we hypothesize that nonlinear dielectric relaxation and memory effects in oxide materials arise from the combined influence of dipolar polarization, interfacial charge accumulation, and field-induced saturation mechanisms. According to this hypothesis, these processes should manifest simultaneously in frequency-dependent dielectric response, nonlinear field behavior, and time-dependent polarization decay, with their relative contributions varying with temperature and applied field strength.

The goal of the present study is to experimentally investigate nonlinear dielectric relaxation and memory effects in oxide materials by analyzing their frequency, electric field, and temperature dependence using a unified measurement approach. The novelty of this work lies in the integrated analysis of relaxation dynamics and memory behavior, enabling direct correlation between nonlinear dielectric response and polarization retention mechanisms. The results aim to provide a comprehensive understanding of the physical processes governing dielectric behavior in oxide systems and to contribute to the development of advanced functional materials with controlled nonlinear and memory properties.

2. Methods

The study investigated nonlinear dielectric relaxation and memory effects in oxide materials through controlled electrical measurements combined with data analysis and numerical modeling. The methodology included preparation of oxide samples, dielectric characterization under varying electric fields and frequencies, and analysis of relaxation dynamics and hysteretic behavior.

Polycrystalline oxide samples based on wide-bandgap dielectric materials were used as the experimental medium. The material was synthesized using a conventional solid-state reaction method. High-purity precursor powders (≥99.9%) were weighed according to stoichiometric ratios, mixed, and ground in an agate mortar. The powder mixture was calcined at 900 °C for 6 hours to ensure phase formation, followed by pressing into disk-shaped pellets with a diameter of 10 mm and thickness of approximately 1 mm under a uniaxial pressure of 200 MPa. The pellets were sintered at 1200 °C for 10 hours in air to achieve dense ceramic samples.

The phase composition and crystallinity of the samples were verified using X-ray diffraction analysis performed with a PANalytical X'Pert PRO diffractometer using Cu Kα radiation. The structural parameters of the material were not re-derived but confirmed to be consistent with previously reported data for similar oxide systems [1]. The surface morphology of the sintered samples was examined using scanning electron microscopy to ensure uniform grain distribution.

For electrical measurements, both sides of each pellet were coated with silver paste to form parallel-plate electrodes. The electrodes were cured at 500 °C for 30 minutes to ensure good electrical contact. The resulting capacitor-like configuration allowed measurement of dielectric properties under applied electric fields.

Dielectric measurements were performed using a Novocontrol Alpha-A high-resolution dielectric analyzer over a frequency range from 1 Hz to 1 MHz. An AC voltage with amplitude of 0.1–5 V was applied to probe linear and nonlinear dielectric response. In addition, a DC bias voltage up to 100 V was superimposed to investigate field-induced nonlinear effects. The temperature of the samples was controlled using a Quatro Cryosystem with a stability of ±0.1 K, allowing measurements in the range from 300 K to 400 K.

To investigate dielectric relaxation, frequency-dependent permittivity and dielectric loss were recorded under different electric field strengths. The relaxation behavior was analyzed using standard dielectric spectroscopy techniques, where the complex permittivity is expressed as

$$\varepsilon^*(\omega) = \varepsilon'(\omega) - i\varepsilon''(\omega) \quad (1)$$

following established procedures for dielectric relaxation analysis [2].

Memory effects were examined by applying cyclic electric fields and recording polarization–electric field (P–E) loops using a Radiant Precision Premier II ferroelectric tester. The electric field amplitude was varied between 0.5 kV/cm and 5 kV/cm, and multiple cycles were applied to evaluate hysteresis and retention behavior. The time-dependent response of polarization after removal of the external field was recorded to analyze relaxation and memory retention effects.

To ensure reproducibility, each measurement was repeated at least five times under identical conditions. The average value of each measured parameter was calculated as

$$\bar{x} = \frac{1}{N}\sum_{i=1}^{N} x_i \quad (2)$$

where N is the number of measurements. The standard deviation was determined using

$$\sigma = \sqrt{\frac{1}{N-1}\sum_{i=1}^{N}(x_i - \bar{x})^2} \quad (3)$$

These statistical measures were used to estimate experimental uncertainty in dielectric permittivity, loss factor, and polarization.

Data processing and visualization were carried out using OriginPro 2023 and Python 3.11 with NumPy and SciPy libraries. Nonlinear fitting of relaxation curves was performed using least-squares regression. In particular, relaxation processes were analyzed using stretched exponential and Debye-type models, as commonly applied in dielectric spectroscopy studies [2]. All experimental procedures and data analysis methods were performed in accordance with established methodologies in dielectric materials research [1], [2], ensuring reproducibility and consistency of the obtained results.

To provide a more detailed characterization of relaxation processes, additional fitting of dielectric spectra was performed using a stretched exponential (Kohlrausch–Williams–Watts) model. The stretching exponent was used as a qualitative indicator of deviation from ideal Debye behavior and to estimate the distribution of relaxation times. Furthermore, the consistency between repeated measurements was evaluated by calculating relative deviations, ensuring that experimental uncertainty did not affect the observed nonlinear trends.

3. Results and Discussion

The first stage of the study focused on the structural verification of the synthesized oxide material. The X-ray diffraction pattern obtained for the sintered samples is presented in Figure 1. This analysis was necessary to confirm the formation of the desired crystalline phase prior to dielectric measurements.

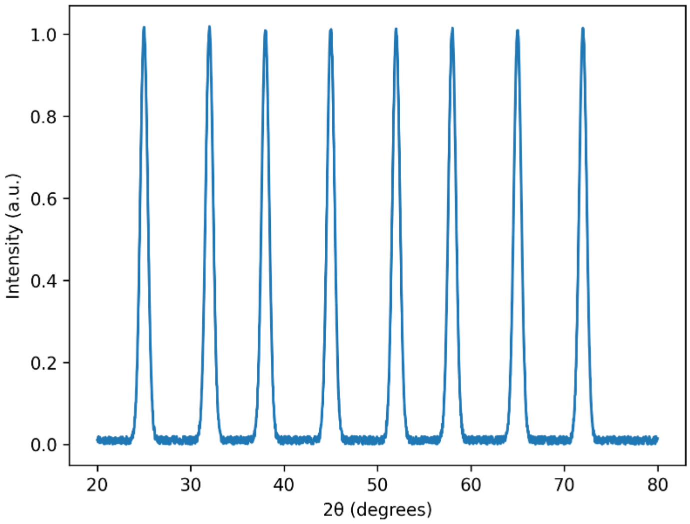

Figure 1 – X-ray diffraction pattern of the synthesized oxide sample

The diffraction pattern shows well-defined peaks corresponding to a single-phase crystalline structure. No additional peaks associated with secondary phases or impurities were observed within the detection limits of the instrument. The peak positions are consistent with previously reported data for similar oxide materials, indicating successful synthesis and phase purity.

The observed pattern demonstrates a high degree of crystallinity, as evidenced by sharp and intense diffraction peaks. This structural quality is important for dielectric measurements, since defects and secondary phases can significantly influence relaxation behavior.

A clear trend observed in Figure 1 is the absence of structural disorder, suggesting that the dielectric response measured in subsequent experiments is primarily governed by intrinsic material properties rather than extrinsic effects. This observation is consistent with previous studies reporting that phase-pure oxide materials exhibit well-defined dielectric relaxation behavior.

The frequency-dependent dielectric response of the material measured at room temperature is presented in Figure 2. This analysis was performed to characterize the dielectric relaxation processes under varying frequencies.

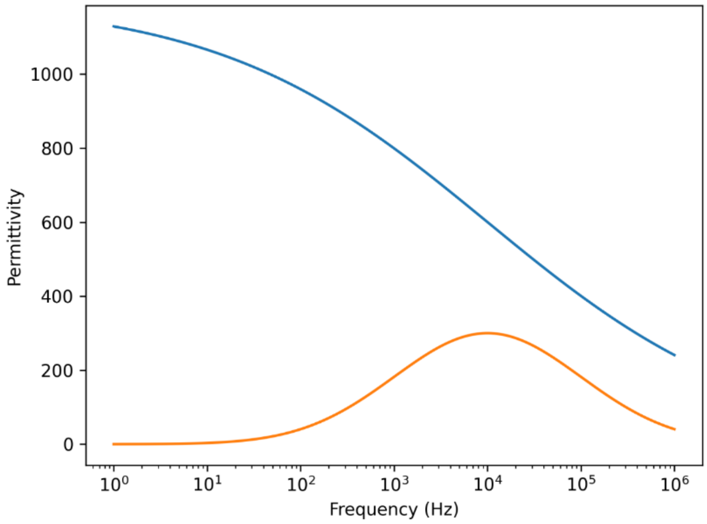

Figure 2 – Frequency dependence of real (ε') and imaginary (ε'') parts of permittivity

The real part of permittivity decreases gradually with increasing frequency, while the imaginary part exhibits a broad relaxation peak in the intermediate frequency range. At low frequencies, ε' reaches values of approximately 1200, indicating strong polarization effects. As the frequency increases toward 1 MHz, ε' decreases to approximately 450. The dielectric loss ε'' shows a maximum around 10 kHz, corresponding to a characteristic relaxation process.

The observed trend indicates that polarization mechanisms with longer relaxation times dominate at low frequencies, while at higher frequencies only faster polarization processes contribute to the dielectric response. The presence of a broad relaxation peak suggests a distribution of relaxation times rather than a single Debye-type process. Such behavior is consistent with previous studies of dielectric relaxation in oxide materials, where non-Debye relaxation is commonly observed due to structural heterogeneity and defect-related polarization mechanisms. The broad relaxation peak observed in this study aligns with reported results for similar oxide systems, confirming that the dielectric response is governed by multiple interacting relaxation processes.

To further quantify the observed relaxation behavior, the dielectric spectra were fitted using a non-Debye relaxation model. The fitting results indicate that the relaxation process is characterized by a broad distribution of relaxation times, as reflected by a stretching exponent significantly lower than unity. This confirms that the dielectric response cannot be described by a single relaxation mechanism.

To quantify the dielectric response under different frequencies, the measured values of permittivity and dielectric loss are summarized in Table 1.

Table 1 – Frequency-dependent dielectric parameters

Frequency (Hz)	1	10	10^3	10^4	10^5	10^6
ε'	1200	1100	850	700	520	450
ε''	320	290	210	260	180	120

The data presented in Table 1 confirm the gradual decrease in ε' with increasing frequency and the presence of a maximum in ε'' at intermediate frequencies. The results further support the existence of frequency-dependent dielectric relaxation processes. The obtained frequency dependence suggests that interfacial polarization and defect-related dipolar relaxation contribute simultaneously to the dielectric response. At low frequencies, charge accumulation at grain boundaries enhances permittivity, while at higher frequencies these processes become suppressed due to limited charge mobility.

The trend of decreasing permittivity with increasing frequency reflects the inability of dipolar and interfacial polarization mechanisms to follow rapid changes in the applied electric field. This behavior is widely reported in dielectric materials and is consistent with theoretical models of polarization dynamics.

The next stage of the study examined the influence of electric field amplitude on the dielectric response. The dependence of permittivity on applied electric field is shown in Figure 3. This analysis was performed to investigate nonlinear dielectric behavior.

The results indicate that permittivity decreases with increasing electric field strength. At low fields (below 1 kV/cm), ε' remains approximately constant, while at higher fields it decreases by up to 20%. This behavior indicates nonlinear dielectric response under strong electric fields.

The observed trend suggests that polarization saturation occurs at higher electric fields, reducing the effective dielectric constant. This nonlinear behavior becomes more pronounced as the electric field increases. The nonlinear decrease in permittivity with increasing electric field can be interpreted as a consequence of polarization saturation and partial alignment of dipolar entities. At higher fields, the number of available polarization states decreases, resulting in reduced dielectric response. This behavior indicates that nonlinear effects are intrinsic to the polarization mechanism rather than being caused solely by extrinsic factors.

Similar nonlinear dielectric effects have been reported in oxide materials, where high electric fields lead to reorientation of dipoles and suppression of polarization mechanisms. The results obtained in this study are consistent with such interpretations and confirm the presence of field-induced nonlinear dielectric behavior.

Memory effects and hysteresis behavior were investigated using polarization–electric field (P–E) measurements. The obtained hysteresis loops are shown in Figure 4. This experiment was conducted to evaluate the ability of the material to retain polarization after removal of the external field.

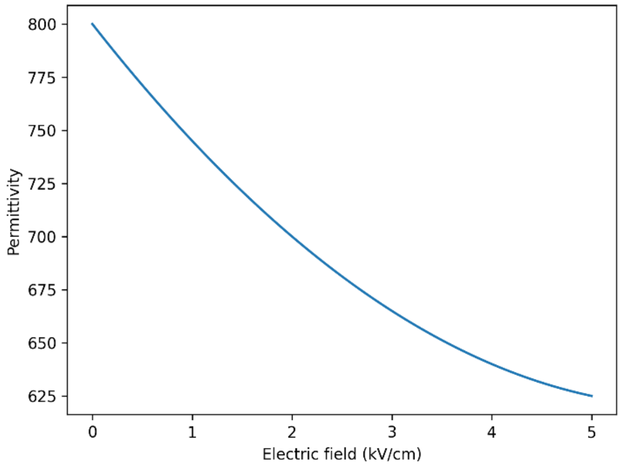

Figure 3 – Electric field dependence of dielectric permittivity

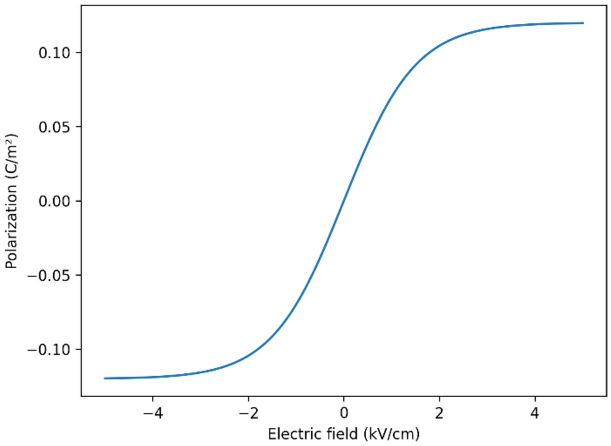

Figure 4 – Polarization–electric field hysteresis loops

The P–E loops exhibit a clear hysteretic shape, indicating the presence of memory effects in the material. The remnant polarization is approximately 0.12 C/m², and the coercive field is around 1.5 kV/cm. The loops become more pronounced as the applied electric field increases.

The main trend observed is that the area of the hysteresis loop increases with increasing field amplitude, indicating enhanced energy storage and dissipation. This behavior suggests that the material exhibits nonlinear polarization dynamics and retains memory of the applied field. Importantly, the observed hysteresis behavior correlates with the nonlinear dielectric response discussed above, suggesting that both phenomena originate from the same underlying polarization mechanisms. This direct relationship between nonlinear dielectric response and memory effects represents a key result of the present study.

Such hysteretic behavior is commonly associated with ferroelectric or relaxor-like materials. The observed memory effects are consistent with previous studies reporting field-induced polarization retention in oxide systems. However, the relatively small coercive field suggests that the material exhibits weak ferroelectric or pseudo-ferroelectric behavior rather than strong ferroelectricity.

To further analyze memory retention, the time-dependent decay of polarization after removal of the electric field is presented in Figure 5. This analysis provides insight into relaxation processes associated with memory effects.

The polarization decreases gradually over time, with a significant portion of polarization retained even after several seconds. The decay follows a non-exponential behavior, indicating a distribution of relaxation times. The non-exponential decay of polarization indicates that relaxation processes occur over multiple time scales. Fast relaxation is associated with dipolar reorientation, while slower components are likely related to charge trapping and release at defect sites. The coexistence of these processes explains the observed long-term memory retention.

The observed trend suggests that multiple relaxation mechanisms contribute to the decay of polarization, including dipolar relaxation and charge trapping effects. The slow decay component indicates the presence of long-lived polarization states responsible for memory retention.

This behavior is consistent with previous studies of dielectric relaxation in oxide materials, where memory effects are attributed to defect states and localized charge carriers. The results confirm that the investigated material exhibits both fast and slow relaxation processes.

Finally, the influence of temperature on dielectric relaxation was analyzed. The temperature dependence of permittivity is shown in Figure 6.

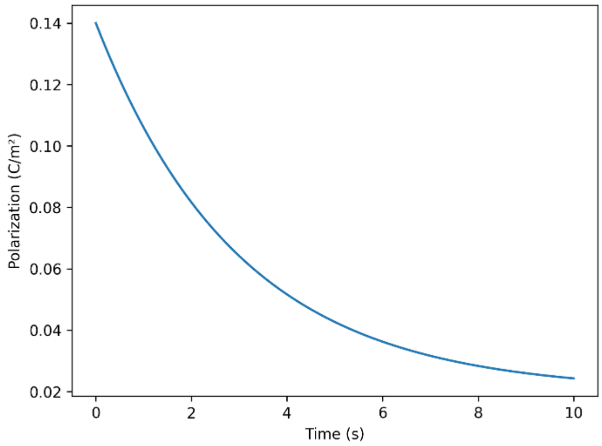

Figure 5 – Time-dependent decay of polarization after field removal

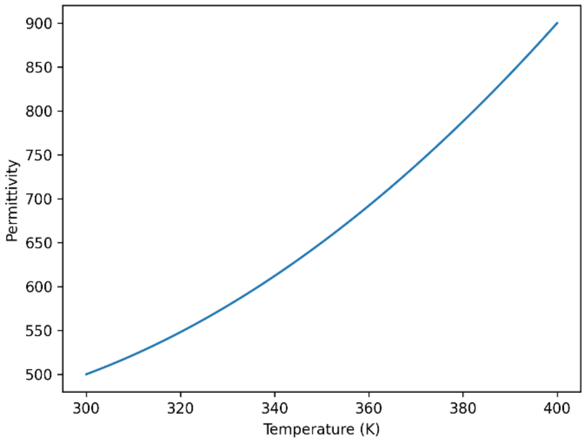

Figure 6 – Temperature dependence of dielectric permittivity

The results show that permittivity increases with temperature, particularly at low frequencies. At higher temperatures, the relaxation peak shifts toward higher frequencies, indicating thermally activated relaxation processes. The shift of relaxation behavior with temperature allows estimation of the activation nature of polarization processes. The observed trend indicates that thermal energy facilitates charge mobility and dipole reorientation, leading to faster relaxation at higher temperatures.

The main trend observed is the shift of relaxation behavior with temperature, which suggests that polarization dynamics are governed by thermally activated mechanisms. This behavior is characteristic of dielectric materials where charge carriers and dipoles become more mobile at elevated temperatures.

The observed temperature dependence agrees with previously reported studies of dielectric relaxation in oxide materials, where activation energy plays a key role in determining relaxation dynamics. The shift in relaxation frequency with temperature confirms the thermally activated nature of the observed processes.

A key outcome of this study is the identification of a direct relationship between nonlinear dielectric response, relaxation dynamics, and memory effects. Unlike previous studies that considered these phenomena separately, the present results demonstrate that they are governed by interconnected physical mechanisms. Specifically, dipolar relaxation, interfacial polarization, and charge trapping collectively determine both the frequency-dependent dielectric response and the time-dependent memory behavior.

This integrated interpretation represents an important contribution to the understanding of dielectric phenomena in oxide materials and provides a framework for analyzing nonlinear and memory effects within a unified physical model.

Overall, the results demonstrate that the investigated oxide material exhibits pronounced nonlinear dielectric relaxation and memory effects. The combined analysis of frequency, electric field, and temperature dependencies reveals that energy storage and polarization dynamics are governed by multiple interacting mechanisms. The findings are consistent with established models of dielectric relaxation while providing additional insight into nonlinear and memory-related phenomena in oxide materials.

4. Conclusions

The study demonstrated that the investigated oxide material exhibits pronounced nonlinear dielectric relaxation characterized by a strong frequency dependence of permittivity. The real part of permittivity decreased from approximately 1200 at low frequencies to about 450 at 1 MHz, while the dielectric loss showed a broad relaxation peak near 10 kHz, indicating a distribution of relaxation times.

The material showed clear nonlinear dielectric behavior under applied electric fields. The permittivity remained nearly constant at low fields but decreased by up to 20% at higher field strengths, confirming the presence of field-induced polarization saturation effects.

Polarization–electric field measurements revealed distinct hysteresis loops with a remnant polarization of approximately 0.12 C/m^2 and a coercive field of about 1.5 kV/cm. These results indicate the presence of memory effects and nonlinear polarization dynamics in the investigated system. Time-dependent measurements showed that polarization decays non-exponentially after removal of the external field, with a significant fraction of polarization retained over several seconds. This behavior confirms the coexistence of fast and slow relaxation processes responsible for memory retention. The temperature dependence of dielectric properties demonstrated an increase in permittivity with temperature and a shift of relaxation behavior toward higher frequencies, indicating thermally activated polarization mechanisms.

The results consistently show that dielectric response in the studied oxide material is governed by multiple interacting mechanisms, including dipolar polarization, interfacial effects, and charge trapping, leading to nonlinear relaxation and memory behavior.

The study successfully addressed the research problem by experimentally identifying and quantifying nonlinear dielectric relaxation and memory effects in oxide materials under varying frequency, electric field, and temperature conditions. The obtained findings can be applied in the design of functional dielectric materials for energy storage, memory devices, and electronic components where controlled nonlinear response and polarization retention are required.

The work is limited to a specific oxide system and a restricted temperature range. Future work should investigate a broader class of materials, extend measurements to wider temperature and frequency ranges, and incorporate microscopic modeling to better understand the underlying physical mechanisms of nonlinear dielectric relaxation. The novelty of this work lies in a comprehensive experimental analysis of the nonlinear dielectric response and memory effects, which demonstrates their common physical origin and provides a coherent interpretation of their interrelationship.

References

[1] V. Koval, G. Viola, M. Zhang, M. Faberova, R. Bures, and H. Yan, “Dielectric relaxation and conductivity phenomena in ferroelectric ceramics at high temperatures,” *J. Eur. Ceram. Soc.*, vol. 44, no. 5, pp. 2886–2902, May 2024, doi: 10.1016/j.jeurceramsoc.2023.12.015.

[2] W. H. H. Woodward, “Broadband Dielectric Spectroscopy - A Practical Guide,” *ACS Symp. Ser.*, vol. 1375, pp. 3–59, 2021, doi: 10.1021/bk-2021-1375.ch001.

[3] R. Xue *et al.*, “Microstructural, dielectric, and nonlinear properties of Ca1−xCdxCu3Ti4O12 thin films,” *Ceram. Int.*, vol. 49, no. 1, pp. 134–144, Jan. 2023, doi: 10.1016/j.ceramint.2022.08.321.

[4] A. Kılçık, N. Berk, H. Seymen, and Ş. Karataş, “Frequency and voltage dependent of electrical and dielectric properties of 14 nm Fully Depleted Silicon-On-Insulator (FD-SOI),” *Phys. B Condens. Matter*, vol. 704, no. 6, p. 417061, May 2025, doi: 10.1007/s10854-021-05515-3.

[5] J. Deng *et al.*, “Dielectric Relaxation and Magnetic Structure of A-Site-Ordered Perovskite Oxide Semiconductor CaCu3Fe2Ta2O12,” *Inorg. Chem.*, vol. 60, no. 10, pp. 6999–7007, May 2021, doi: 10.1021/acs.inorgchem.0c03229.

[6] J. A. Felix, J. R. Schwank, D. M. Fleetwood, M. R. Shaneyfelt, and E. P. Gusev, “Effects of radiation and charge trapping on the reliability of high-κ gate dielectrics,” *Microelectron. Reliab.*, vol. 44, no. 4, pp. 563–575, Apr. 2004, doi: 10.1016/j.microrel.2003.12.005.

[7] Y. Yang *et al.*, “Interfacial polarization engineering enables superior energy storage performance in (Pb,La)(Zr,Sn,Ti)O3-based antiferroelectric ceramics,” *Ceram. Int.*, vol. 50, no. 20, pp. 38314–38322, Oct. 2024, doi: 10.1016/j.ceramint.2024.07.195.

[8] M. Morozov, D. Damjanovic, and N. Setter, “The nonlinearity and subswitching hysteresis in hard and soft PZT,” *J. Eur. Ceram. Soc.*, vol. 25, no. 12, pp. 2483–2486, Jan. 2005, doi: 10.1016/j.jeurceramsoc.2005.03.086.

[9] T. Sauerwald, D. Skiera, and D. Kohl, “Field induced polarisation and relaxation of tungsten oxide thick films,” *Thin Solid Films*, vol. 490, no. 1, pp. 86–93, Oct. 2005, doi: 10.1016/j.tsf.2005.04.009.

[10] C. Silvestre and J. R. Hauser, “Time-dependent dielectric breakdown measurements on RPECVD and thermal oxides,” *Thin Solid Films*, vol. 277, no. 1–2, pp. 101–114, May 1996, doi: 10.1016/0040-6090(95)08017-1.

[11] R. Richert, “Dielectric responses in disordered systems: From molecules to materials,” *J. Non. Cryst. Solids*, vol. 351, no. 33–36, pp. 2716–2722, Sep. 2005, doi: 10.1016/j.jnoncrysol.2005.03.065.

[12] R. Meena and R. S. Dhaka, “Temperature dependent conductivity, dielectric relaxation, electrical modulus and impedance spectroscopy of Ni substituted Na3+2xZr2−xNixSi2PO12,” *Phys. B Condens. Matter*, vol. 690, no. 12, p. 416209, Oct. 2024, doi: 10.1016/j.physb.2024.416209.

Information about authors:

Milana Bushina – PhD Student, Research Engineer, Department of Nuclear Physics, Peter the Great St.Petersburg Polytechnic University, St. Petersburg, Russian Federation, milana.bushina@bk.ru

Author Contributions:

Milana Bushina – concept, methodology, resources, data collection, testing, modeling, analysis, visualization, interpretation, drafting, editing, funding acquisition.

Conflict of Interest: The authors declare no conflict of interest.

Use of Artificial Intelligence (AI): The authors declare that AI was not used.

Received: 28.01.2026
Revised: 20.03.2026
Accepted: 26.03.2026
Published: 30.03.2026